

Review

Mechanistic Insights into Photodegradation of Organic Dyes Using Heterostructure Photocatalysts

Yi-Hsuan Chiu ¹, Tso-Fu Mark Chang ^{2,*}, Chun-Yi Chen ^{2,*}, Masato Sone ²
and Yung-Jung Hsu ^{1,3,*}

¹ Department of Materials Science and Engineering, National Chiao Tung University, Hsinchu 30010, Taiwan; chiuyhs@gmail.com

² Institute of Innovative Research, Tokyo Institute of Technology, 4259 Nagatsuta-cho, Midori-ku, Yokohama 226-8503, Japan; sone.m.aa@m.titech.ac.jp

³ Center for Emergent Functional Matter Science, National Chiao Tung University, Hsinchu 30010, Taiwan

* Correspondence: chang.m.aa@m.titech.ac.jp (T.-F.M.C.); chen.c.ac@m.titech.ac.jp (C.-Y.C.); yhsu@cc.nctu.edu.tw (Y.-J.H.)

Received: 12 April 2019; Accepted: 3 May 2019; Published: 9 May 2019



Abstract: Due to its low cost, environmentally friendly process, and lack of secondary contamination, the photodegradation of dyes is regarded as a promising technology for industrial wastewater treatment. This technology demonstrates the light-enhanced generation of charge carriers and reactive radicals that non-selectively degrade various organic dyes into water, CO₂, and other organic compounds via direct photodegradation or a sensitization-mediated degradation process. The overall efficiency of the photocatalysis system is closely dependent upon operational parameters that govern the adsorption and photodegradation of dye molecules, including the initial dye concentration, pH of the solution, temperature of the reaction medium, and light intensity. Additionally, the charge-carrier properties of the photocatalyst strongly affect the generation of reactive species in the heterogeneous photodegradation and thereby dictate the photodegradation efficiency. Herein, this comprehensive review discusses the pseudo kinetics and mechanisms of the photodegradation reactions. The operational factors affecting the photodegradation of either cationic or anionic dye molecules, as well as the charge-carrier properties of the photocatalyst, are also fully explored. By further analyzing past works to clarify key active species for photodegradation reactions and optimal conditions, this review provides helpful guidelines that can be applied to foster the development of efficient photodegradation systems.

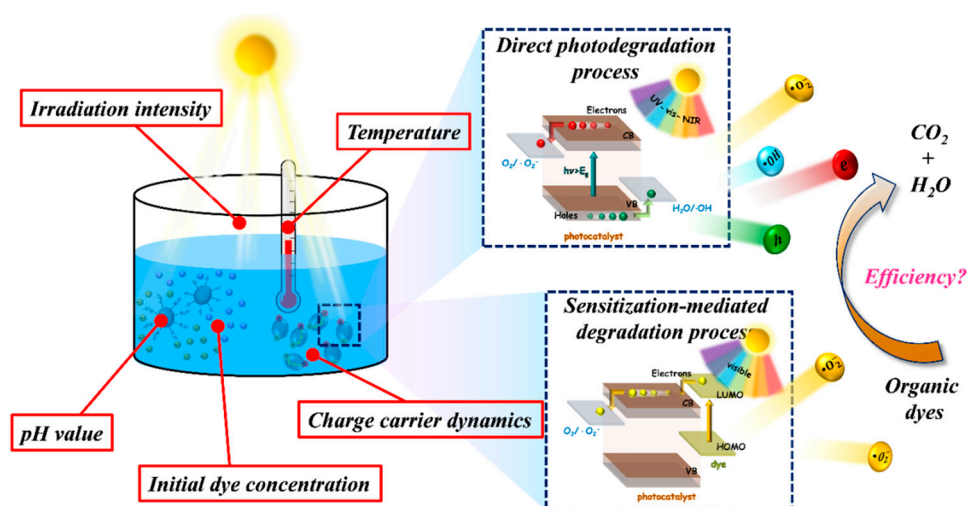
Keywords: cationic dye; anionic dye; direct photoderadation; sensitization-mediated degradation; quantum yield

1. Introduction

The widespread presence of organic dyes in industrial wastewaters from the textile, apparel, and paper industries results in significant environmental contamination. These dye-polluted effluents contain highly hazardous, carcinogenic, non-biodegradable, and colored pigments that can cause damage to humans [1,2]. Even at very low concentrations (below 1 ppm), dyes are clearly visible in water and seriously deteriorate aqueous environments [3–5]. Therefore, the removal of colored organic dyes from wastes is imperative and important. For conventional treatment on industrial wastewater, adsorption [6] and coagulation [7] are common methods used to remove the organic dyes. However, these processes cause secondary hazardous pollution because dyes are only changed from a liquid phase into a solid phase. Thus, further treatments are necessary to resolve the problem of secondary pollution [8,9]. Over the past few years, photocatalysis was regarded as a promising

alternative treatment in the aspect of water purification [10]. Essentially, the photocatalytic reaction involves heterogeneous catalysis, where a light-absorbing catalyst is put in contact with the target reactants, in either a solution or gas phase. This heterogeneous approach was successfully employed as an effective tool for the degradation of various hazardous materials, including atmospheric and aquatic organic pollutants, and shows many advantages over traditional wastewater treatment techniques. For instance, the complete degradation of organic pollutants using active photocatalysts can occur within a few hours at room temperature. In addition, organic pollutants can be entirely mineralized to relatively non-toxic products (CO_2 and water) without the formation of secondary hazardous products [11,12].

The typical mechanism for the photodegradation of organic dyes is shown in Scheme 1. Upon irradiation with incident photons, electrons are excited to the conduction band (CB) of the photocatalyst, while holes are formed in the valance band (VB). The photoexcited electrons and holes can either recombine to generate thermal energy or diffuse to the photocatalyst surface reacting with the adsorbed molecules. The reactive radical species, such as superoxide radicals ($\cdot\text{O}_2^-$) and hydroxyl radicals ($\cdot\text{OH}$), are further derived from the photoexcited electrons and holes, respectively. Moreover, the photosensitization of dye molecules can provide photocatalysts with additional electrons, which are also capable of generating radicals like $\cdot\text{O}_2^-$. These reactive species can quickly and non-selectively decompose organic pollutants. The whole photodegradation process, from the adsorption of dye molecules on the surface of the photocatalyst to the decomposition of dye molecules by reactive radicals, is affected by operational parameters such as the pH of solution, initial dye concentration, reaction temperature, and irradiation intensity [13–17]. For example, Neppolian et al. reported that the degradation of reactive yellow 17, reactive red 2, and reactive blue 4 over Degussa P-25 followed pseudo first-order kinetics [14], in which increasing initial dye concentration depressed the photodegradation efficiency. Shahwan et al. performed photodegradation of methyl blue and methyl orange [13], and found that the pH of solution and steric structure were highly related to photocatalytic efficiency. In addition to these operational parameters, the band position and charge-carrier utilization of the photocatalysts also have an impact on the generation of reactive radicals and the subsequent photodegradation performance. To improve the carrier utilization and thereby achieve efficient reactive radical generation, heterostructure photocatalysts with enhanced photocatalytic activity are proposed and employed [18–25].



Scheme 1. Schematic illustration of operational factors affecting the photodegradation of organic dyes over semiconductor photocatalysts.

This comprehensive review discusses the pseudo kinetics and mechanisms for photodegradation reactions. The operational factors affecting the photodegradation of either cationic or anionic dye molecules, as well as the charge-carrier properties of the photocatalysts, are also fully explored. Finally, we outline earlier works to reveal the key reactive species accounting for the photodegradation of

different dyes, providing helpful guidelines that could be applied to foster the development of efficient photodegradation systems.

2. Classification of Organic Dyes

Basically, the chemical structure of dye molecules determines their color and properties. Therefore, they can be classified according to their chemical structure (functional groups), color, or aspects of usage [26]. In the textile industry, commonly used dyes include acid, basic, direct, azo, naphtha, reactive, mordant, vat, disperse, and sulfur dyes [27], with azo dyes being the most used at present. To study their properties with regard to photodegradation reactions, dyes are usually classified using their molecular charge upon dissociation in aqueous-based applications. Table 1 presents the chemical properties of several representative dyes that are frequently used in photodegradation applications. According to the chemical structure, they are divided into cationic and anionic dyes. The cationic dyes, including methylene blue (MB), rhodamine B (RhB), malachite green (MG), rhodamine 6G (Rh6G), crystal violet (CV), and safranin O (SO), contain cationic functional groups that can dissociate into positively charged ions [28] in an aqueous solution. The most common cationic functional group is the onium group and, thus, most of the cations are N^+ ions. On the other hand, the anionic dyes cover direct, acid, and reactive dyes [29], such as acid orange 7 (AO7), eosin Y (EY), methyl orange (MO), acid red 14 (AR14), alizarin red S (ARS), rose bengal (RB), and phenol red (PR). All anionic dyes contain anionic functional groups, e.g., sulfonic or carboxylic acid groups [5]. These functional groups are water-soluble and can effectively interact with photocatalysts with hydrophilic surfaces. Hence, cationic and anionic dyes are also known as basic and acidic dyes, respectively.

Table 1. Chemical properties of representative cationic and anionic dyes. M_W —molecular weight.

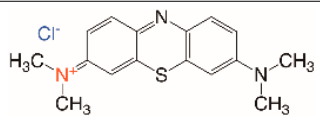
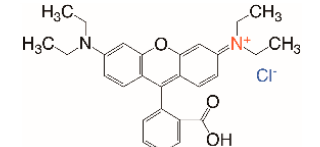
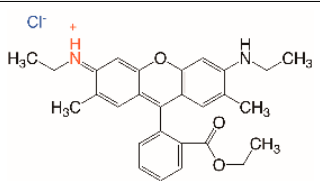
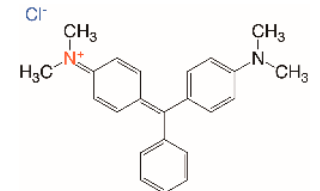
Cationic Dyes	Abbreviation	M_W	Structure	λ_{max} (nm)
Methylene blue	MB	799.81		664
Rhodamine B	RhB	479.02		553
Rhodamine 6G	Rh6G	479.02		534
Malachite green	MG	364.91		614

Table 1. Cont.

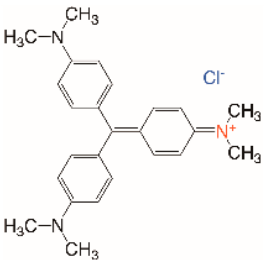
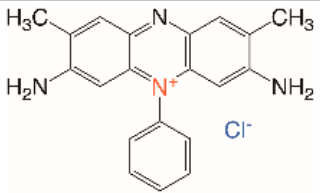
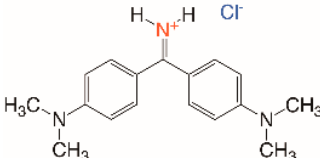
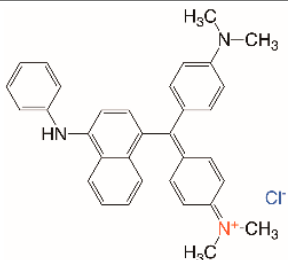
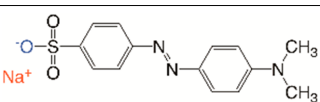
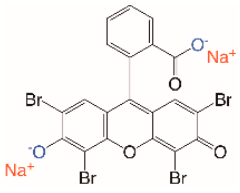
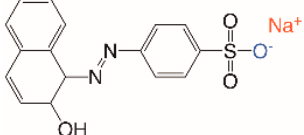
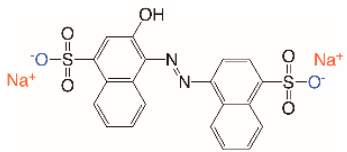
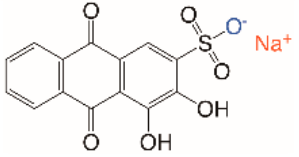
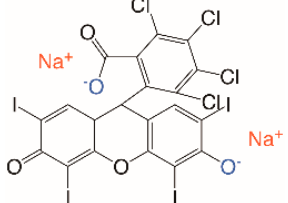
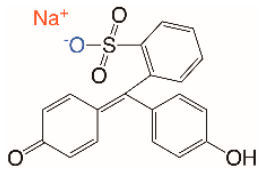
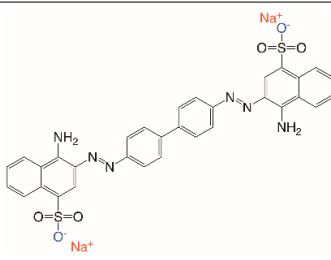
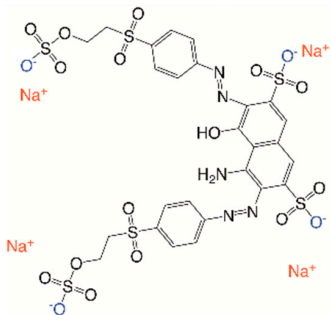
Cationic Dyes	Abbreviation	M _W	Structure	λ _{max} (nm)
Crystal violet	CV	407.98		573
Safranin O	SO	350.85		520
Auramine O	AO	303.83		420
Victoria blue B	VBB	506.08		614
Anionic Dyes	Abbreviation	M _w	Structure	λ _{max} (nm)
Methyl orange	MO	327.33		464
Eosin Y	EY	691.85		518
Acid orange 7	AO7	350.32		484

Table 1. Cont.

Anionic Dyes	Abbreviation	Mw	Structure	λ_{max} (nm)
Acid red 14	AR14	502.43		515
Alizarin red S	ARS	240.21		426
Rose bengal	RB	973.67		550
Phenol red	PR	354.38		560
Congo red	CR	696.67		497
Acid violet 7	AV7	566.47		522
Reactive black 5	RB5	991.82		602

3. Kinetics Study for Photodegradation Reactions

The kinetics for photodegradation reactions are examined based on the dye concentration change by measuring the characteristic absorbance peak at different irradiation times. All the common dyes have their specific characteristic absorptions in the visible range (400–700 nm), as shown in Table 1. Herein, the efficiency of photodegradation (also known as the decolorizing ratio) is determined using the following equation:

$$\text{Degradation Efficiency (\%)} = \frac{C_0 - C}{C_0} \times 100, \quad (1)$$

where C_0 and C are the solution concentration at $t = 0$ and after some irradiation time. However, the absorption peak shift or excitation of the dye molecules may cause the inaccurate estimation of the photodegradation efficiency, which is further discussed in Sections 3.1 and 3.2.

3.1. Absorption Peak Shift of Dye Molecules

During the photodegradation reaction, a redshift or blueshift can be sometimes seen in the characteristic absorption of dye molecules, possibly caused by the aggregation of organic dyes [13,30]. Furthermore, the decomposition process of dye molecules could also cause an absorption peak shift. These spectral shifts bring difficulty in determining the concentration of the remaining dyes from the absorbance of the characteristic peak. Special care is, therefore, necessary in order to represent accurate photodegradation efficiency. As shown in Figure 1a, a typical example can be found for RhB photodegradation on Ag_3PO_4 nanoparticles [31]. The blueshift of the absorption band from 554 to 530 nm was caused by the de-ethylation of RhB molecules. The generation of intermediates can be further observed by steady-state photoluminescence (PL) spectroscopy in Figure 1b. The emission at 575 nm decreased, while a new emission appeared after 7 min of light illumination, confirming the formation of the de-ethylated intermediate. Figure 1c shows the de-ethylation process of RhB molecules. Upon light illumination, the four ethyl groups of RhB can be sequentially removed until it is totally converted into rhodamine without any ethyl groups. This process causes a large blueshift in absorption from 553 nm to 498 nm [32,33], as shown in Figure 2d. The further decomposition of rhodamine with its conjugated ring structure causes a further decrease of the absorption peak without a corresponding peak shift [34]. In the presence of benzoquinone (BQ) as an $\cdot\text{O}_2^-$ scavenger (see Section 5.1), the peak intensity decreases without shifting, while the peak shows a blueshift in the presence of 2-propanol (IPA) as an $\cdot\text{OH}$ scavenger, further confirming that the blueshift is caused by the attack of active oxygen species on the *N*-ethyl groups. Moreover, it was found that the formation of *N*-de-methylated MG products through the attack of active oxygen species accounts for the observed absorption blueshift of the MG absorption during the MG photodegradation over TiO_2 [35].

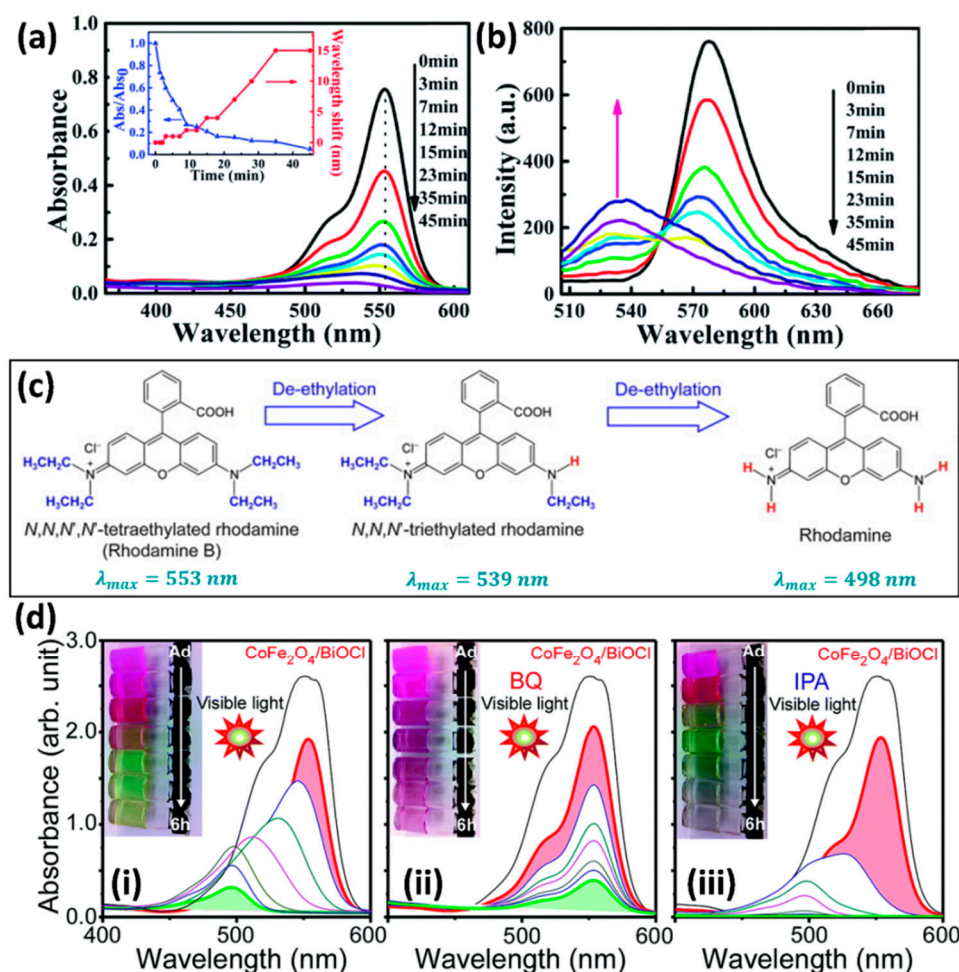


Figure 1. Photodegradation of RhB over Ag_3PO_4 nanoparticles under visible illumination recorded as (a) ultraviolet–visible light (UV–Vis) absorption spectra (inset shows the correlation between absorbance changes of maxima absorption peak (blue line) and the corresponding wavelength shifts (red curve)), and (b) steady-state PL spectra. (reproduced with permission from [31]. Copyright Royal Society of Chemistry, 2017). (c) Scheme of the de-ethylation process of RhB molecules. (d) Photodegradation of RhB over $\text{CoFe}_2\text{O}_4/\text{BiOCl}$ microflowlers under visible irradiation (i) without and with scavengers of (ii) BQ and (iii) IPA. (inset shows photographs of color change of dye molecules with photodegradation time; reproduced with permission from [34]. Copyright Royal Society of Chemistry, 2015).

3.2. Photobleaching of Dye Molecules

The direct excitation of dye molecules may induce the formation of colorless and unstable transition forms, instead of complete mineralization, especially in the presence of dissolved oxygen, which also causes the inaccurate estimation of the photocatalytic activity. Taking the TiO_2/MB system as an example [36], the photoexcited electrons within TiO_2 can transform blue MB molecules into their colorless leuco form (LMB) upon UV irradiation, resulting in the photobleaching of MB (step i), as shown in Figure 2a. In an oxygen-free atmosphere (N_2) without UV irradiation, the bleached condition persists (step ii), with the formation of the stable LMB. In contrast, recoloration takes place if the system is exposed to air (step iii), leading to back electron transfer from LMB to electron acceptors, and causing a reversion to the blue oxidized form of MB. As shown in Figure 2b, the recovery process becomes faster in an oxygen atmosphere (step iv), revealing the recovery rate is proportional to the level of O_2 [37]. A similar observation can be found in the carbon-doped TiO_2/MB system [38]. As Figure 2c shows, under UV irradiation, the excitation of TiO_2 makes the photobleaching reaction (step 1) become dominant. On the other hand, visible light irradiation can drive self-catalyzed LMB oxidation to MB,

thus dramatically enhancing the recoloration rate (step 3). A competing reaction (step 4) usually exists due to the visible photoactivity of carbon-doped TiO₂, whereas this reaction is drastically suppressed in the presence of O₂; thus, the oxidative LMB to MB transition is predominant under visible irradiation in O₂ atmosphere. Thus, the transformation of MB and LMB can be achieved and repeated by changing the irradiation from UV to visible light, as shown in Figure 2d. This photobleaching phenomenon and recovery process was also found for RhB. The recoloration of RhB from leuco RhB (LRhB) can be observed in 55 min of visible irradiation, and the decoloration–recoloration process can be repeated under sequential UV and visible light irradiations (Figure 2e).

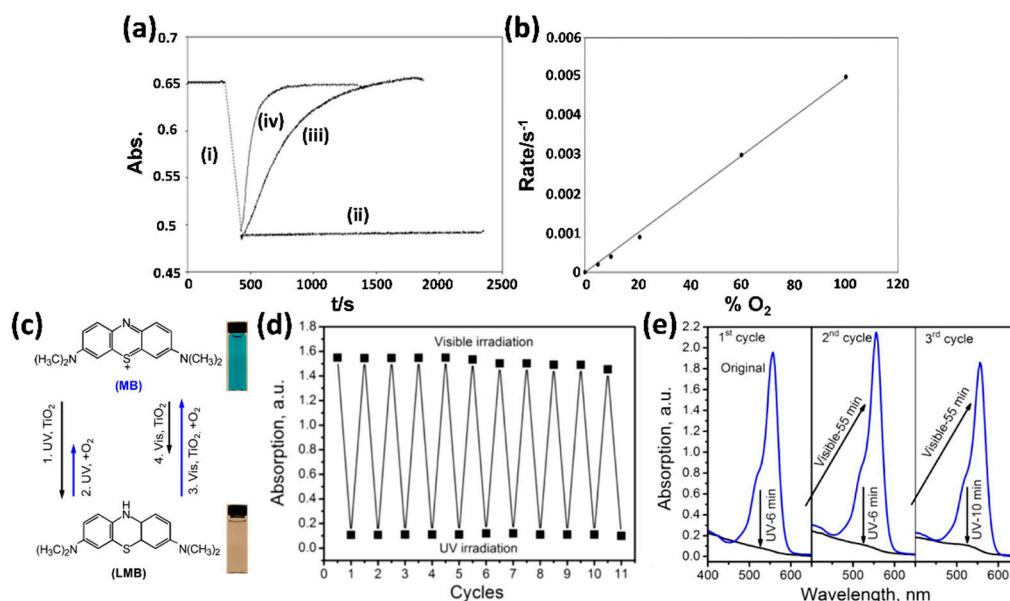


Figure 2. (a) UV–Vis absorption spectra of the TiO₂/MB system upon irradiation for 2.5 min (i) with UV-A light and in (ii) N₂, (iii) air, and (iv) O₂ atmospheres. (reproduced with permission from [36]. Copyright Royal Society of Chemistry, 2004). (b) Change of recovery rate with the O₂ content (reproduced with permission from [37]. Copyright American Chemical Society, 2005). (c) Schematic illustration for photoreversible color switching between MB (blue) and its leuco form (LMB, colourless) on carbon-doped TiO₂ nanocrystals. Test of photoreversible color switch of (d) MB and (e) RhB on carbon-doped TiO₂ nanocrystals under repeated UV and visible irradiation. (reproduced with permission from [38]. Copyright American Chemical Society, 2014).

3.3. Chemical Oxygen Demand (COD) and Total Organic Carbon (TOC) Analysis

To precisely evaluate the extent of decomposition of organic dye molecules during photodegradation, COD and TOC analyses are usually utilized. COD is an indicative measure of oxygen amount that is consumed by oxidation reactions in the solution, which can be used to deduce the number of organic molecules in water. TOC on the other hand is an indicative measure of carbon amount in organic compounds, which can more accurately reflect the total amount of organic compounds in the solution. As shown in Figure 3, the photodegradation of bisphenol A (BPA) was demonstrated using BiOI as photocatalysts [39]. The morphology of BiOI with two specific facets ((110) and (001)) is shown in Figure 3a. Under visible irradiation, BiOI-110 exhibited better photodegradation efficiency than BiOI-001 did because it has a higher capability of adsorbing O₂, thereby facilitating the generation of reactive radicals. The TOC value of the BiOI-110 system decreased to 5% of the initial TOC value, indicating almost complete mineralization of BPA. In contrast, the TOC value of the BiOI-001 system was reduced by only 44%. This observation is consistent with the change in the photodegradation results. Zhao et al. reported the photodegradation of anionic sulforhodamine B (SRB) over TiO₂-Pt photocatalysts [40] under visible irradiation, in which TiO₂-Pt (0.2 wt.%) showed the fastest photodegradation rate, capable of degrading SRB molecules within 130 min (Figure 3d).

To confirm the mineralization of SRB, Figure 3e,f respectively show the temporal changes of COD and TOC during the SRB photodegradation. In the presence of TiO₂/Pt, approximately 64% of the total COD was reduced after 210 min of irradiation. Conversely, the SRB/TiO₂ system required a much longer irradiation time (around 480 min) to attain a similar decrease. In both cases, the COD remained constant with further irradiation, indicating the total discoloration of SRB molecules. This observation was consistent with the changes in TOC. TOC's increase in the first hour of irradiation is due to photodesorption of the dye or the formation of intermediates. After a gradual decrease to the steady state, the TOC remained unchanged because the degraded fragments were not further decomposed with longer irradiation.

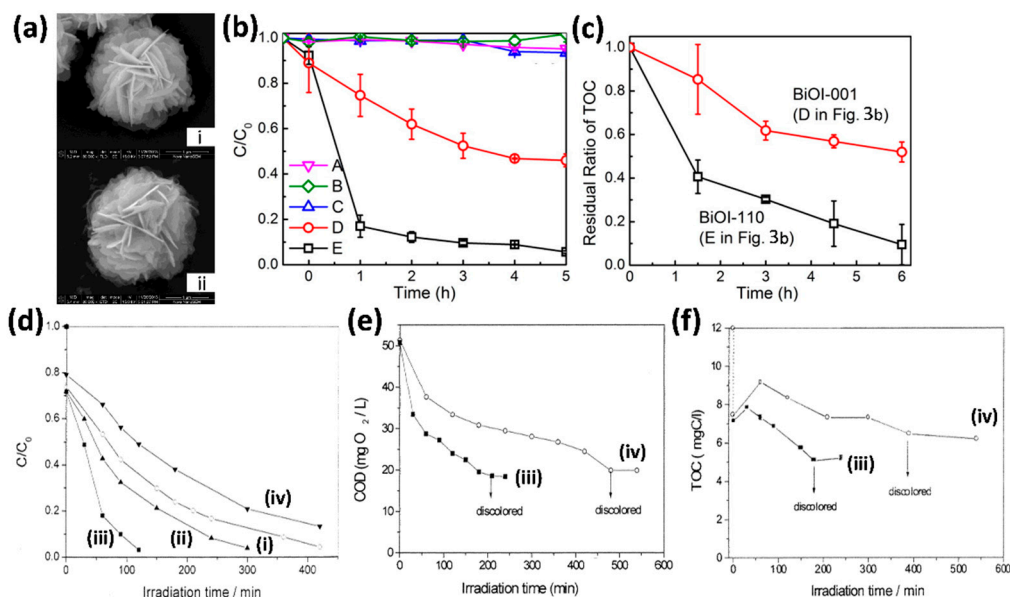


Figure 3. (a) TEM images of (i) BiOI-110 and (ii) BiOI-001. (b) Photodegradation of BPA and (c) reduction of TOC under different conditions: A—without photocatalyst and visible light, B—with BiOI-001 in the dark, C—with BiOI-110 in the dark, D—with BiOI-001 and visible light, and E—with BiOI-110 and visible light (reproduced with permission from [39]. Copyright American Chemical Society, 2015). (d) Photodegradation of SRB and changes in (e) COD and (f) TOC under light irradiation over (i) TiO₂, (ii) TiO₂-Pt (0.1 wt.%), (iii) TiO₂-Pt (0.2 wt.%), and (iv) TiO₂-Pt (0.5 wt.%) (reproduced with permission from [40]. Copyright American Chemical Society, 2002).

3.4. Pseudo Kinetics

To quantify the heterogeneous photodegradation activity, the Langmuir–Hinshelwood (L-H) model is usually considered, as shown in Equation (2).

$$-\frac{dC}{dt} = \frac{kKC}{1 + KC} \quad (2)$$

where K and k are the thermodynamic adsorption constant and photodegradation rate constant, respectively. Because one of the reactants acts as a photocatalyst whose concentration remains unchanged, the reaction kinetics can be simplified, and the term “pseudo” is used to prefix the reaction rate expression. At high concentrations of dye, the photocatalyst surfaces are fully covered, leading to the approximation of $(1 + KC)$ to KC . A pseudo zero-order reaction is, thus, observed for saturation coverage on the surface of the photocatalyst [41], since the photodegradation rate is independent of the change in the dye concentration, as shown in Equation (3).

$$-\frac{dC}{dt} = k. \quad (3)$$

Integrating the equation under the boundary conditions $C = C_0$ at $t = 0$ and $C = \frac{1}{2}C_0$ at $t = t_{1/2}$ respectively yields

$$C_0 - C = k_0t, \quad (4)$$

$$t_{1/2} = \frac{C_0}{2k}. \quad (5)$$

A plot of $C_0 - C$ vs. irradiation time gives a slope equal to the zero-order rate constant (k_0). Additionally, the half-life ($t_{1/2}$) is the time required to photodegrade half of the initial dye concentration, which is used to quantitatively compare the photodegradation reaction. Therefore, the zero-order $t_{1/2}$ can be expressed by Equation (5), and it increases with the initial concentration of dye molecules. On the other hand, at low initial concentrations of dye molecules, i.e., $(KC + 1)^{-1}$, a pseudo first-order rate expression is obtained [42], as shown in Equation (6). The equation is valid by assuming the driving force of degradation is constantly proportional to the dye concentration.

$$-\frac{dC}{dt} = k_1C, \quad (6)$$

where k_1 corresponds to the first-order rate constant. Integrating the equation under the two boundary conditions yields

$$\ln\left(\frac{C_0}{C}\right) = k_1t, \quad (7)$$

$$t_{1/2} = \frac{\ln 2}{k} = \frac{0.6932}{k}. \quad (8)$$

The linear region can be obtained from the plot of $\ln(C_0/C)$ vs. irradiation time, in which the slope gives the rate constant of photodegradation. This model is the most common one used to represent the entire photodegradation process. Here, the half-life is derived from Equation (8). Obviously, the $t_{1/2}$ of the first-order model is independent of the dye concentration.

Conversely, Kumara et al. reported that the photodegradation of AO over ZnO photocatalysts followed second-order kinetics [43]. A second-order reaction in which a single reactant is involved is characterized by the chemical reaction ($2C \rightarrow \text{products}$).

At equilibrium, the second-order kinetics depends on the amount of dye molecules adsorbed on the photocatalyst surface, which is calculated as follows:

$$-\frac{dC}{dt} = k_2C^2. \quad (9)$$

Similarly, by integrating the equation under the two boundary conditions, the second-order rate constant (k_2), as well as $t_{1/2}$, can be obtained. The second-order $t_{1/2}$ increases as the initial concentration is decreased.

$$\frac{1}{C} - \frac{1}{C_0} = k_2t; \quad (10)$$

$$t_{1/2} = \frac{1}{kC_0}. \quad (11)$$

3.5. Quantum Yield of Photodegradation

The photodegradation efficiency is difficult to directly compare with other reported values, since the photodegradation rate constant is affected by various operational effects (see Section 4). In order to objectively estimate the efficiency of the photodegradation reaction, quantum yield (ϕ) is used and defined as the number of reacted charge carriers for dye molecule decomposition per absorbed photon. The apparent quantum yield (AQY) on the other hand is calculated by dividing the number of charge carriers participating in degrading dye molecules by the incident photons. Because the absorbed photons are a certain fraction of the incident photons, the ϕ value is basically higher than the AQY. Bora et al. estimated the AQY of MB photodegradation over Au nanoparticle-decorated ZnO nanorods

(Au–ZnO NRs) [44]. The morphology of Au–ZnO is shown in Figure 4a. It was reported that the photodegradation of MB is initiated by accepting one electron to form semi-reduced MB, followed by further accepting one electron to produce LMB. As a result, two electrons are required for the complete degradation of MB molecules, and the AQY of MB photodegradation can be calculated as follows:

$$\begin{aligned} \text{AQY}(\%) &= \frac{2 \times \text{number of MB molecules}}{\text{number of incident photons}} \times 100\% \\ &= \frac{2n_{\text{MB}}N_{\text{A}}hc}{P_{\text{light}}S\lambda t} \times 100\%, \end{aligned} \quad (12)$$

where n_{MB} (mol) stands for the amount of MB degraded during the irradiation period, N_{A} (mol^{-1}) is Avogadro's constant, P_{light} (W/m^2) is the incident power density, S (m^2) is the irradiation area, t (s) is irradiation time, h is Planck's constant, and λ is the wavelength of incident light. As shown in Figure 4b, all the AQY values of Au–ZnO from 300 to 600 nm were higher than those of bare ZnO NRs and MB only, which was ascribed to the enhanced charge separation at the Au–ZnO interface. The highest AQY value obtained from Au–ZnO exceeded 30% in the UV region, while the bare ZnO NRs showed fairly low photodegradation activity in the visible region and almost no activity at wavelength longer than 450 nm. On the other hand, Au–ZnO NRs showed a six-fold increase of AQY over bare ZnO NRs in the visible region, which can be attributed to the plasmonic effect of Au. In addition, the BiOBr/Bi₂O₃ heterostructures were demonstrated for photodegradation of an RhB/*p*-cresol mixture [45]. The SEM image showed that the composites comprised BiOBr platelets arranging in whorls perpendicular to the Bi₂O₃ surface (Figure 4c). Under blue light-emitting diode (LED) light (430–470 nm) irradiation, the AQY value of *p*-cresol photodegradation in the mixture was substantially higher than the value of RhB due to the carrier transfer from RhB to the co-adsorbed *p*-cresol. Note that there is no photobleaching of RhB as the RhB is unable to absorb blue light (Figure 4d).

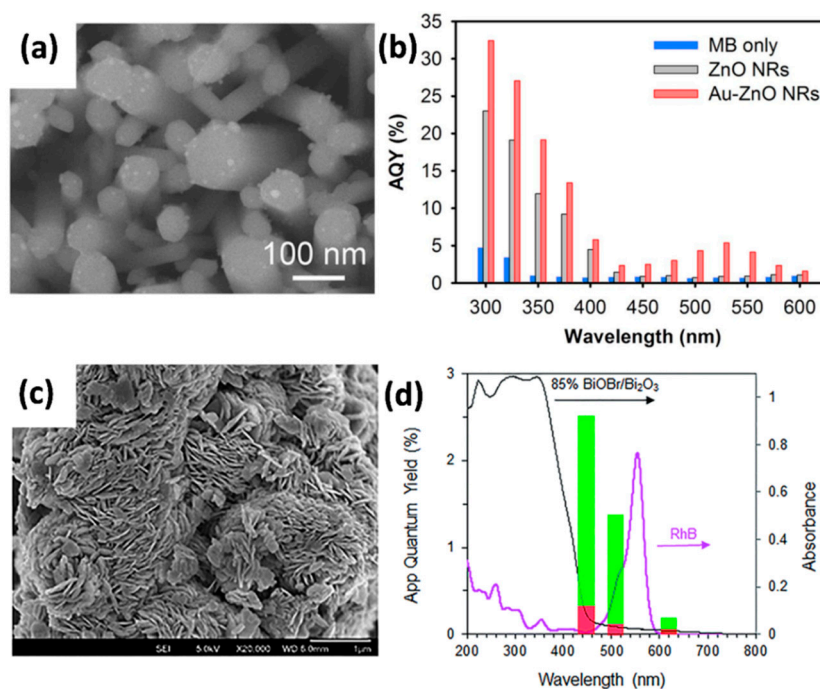


Figure 4. (a) SEM image of Au–ZnO and (b) AQY of MB photodegradation on MB only, ZnO NRs, and Au–ZnO NRs in the wavelength range from 300–600 nm (reproduced with permission from [44]. Copyright Nature Publishing Group, 2016). (c) SEM image of BiOBr/Bi₂O₃ composites and (d) the corresponding AQY of RhB (red) and *p*-cresol (green) photodegradation under blue, green, and red light-emitting diode (LED) light irradiation (reproduced with permission from [45]. Copyright Royal Society of Chemistry, 2017).

In addition, Shams-Ghahfarokhi et al. reported the calculation of the ϕ value from the first-order rate constant of photodegradation process [15,46] using the following equation:

$$\phi = \frac{k_1}{2.303 \times I_{0,\lambda} \times \varepsilon_\lambda \times l'} \quad (13)$$

where k_1 (s^{-1}) stands for the photodegradation first-order rate constant, $I_{0,\lambda}$ (Einstein $l^{-1}s^{-1}$) is the incident intensity at wavelength λ , ε_λ ($cm^{-1}M^{-1}$) represents the molar absorptivity at wavelength λ , and l states the cell path length (cm).

4. Factors Influencing the Photodegradation Reaction

A heterogeneous photocatalytic reaction is composed of two consecutive steps. Firstly, dye molecules interact with the photocatalyst and are adsorbed onto its surface; then, the photodegradation of the dye commences. The overall efficiency of a photocatalysis system is closely dependent on operational parameters that dictate the adsorption and photodegradation of dye molecules. Herein, possible factors affecting the photodegradation reactions are discussed in detail.

4.1. Interaction between Dye Molecules and Photocatalysts

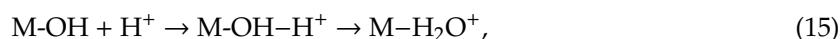
Adsorption is the initial step of the photodegradation reaction prior to the decoloration of dye molecules, which is, thus, an important process for initiating the photodegradation reaction. Both the surface of the photocatalyst and the structure of the dye molecule affect their interactions. Two of the most important interactions between the dye molecules and the photocatalysts are direct bonding and electrostatic interactions. Chemical bonding between functional groups of the dyes and the surface sites of the photocatalysts is a strong interaction to anchor dyes on to photocatalysts [47,48]. For example, RhB with a carboxylic group was demonstrated to bond onto the surface hydroxyls of TiO_2 via an esterification reaction [48]. On the other hand, dye adsorption via electrostatic interaction depends on the nature of dyes, surface properties of photocatalysts, and solution pH. Essentially, the dye adsorption is determined by the strength of the ionic interactions between photocatalysts and dye molecules. An aqueous solution containing salts has a certain value of ionic strength (I), which is defined as

$$I = \frac{1}{2} (C_1 z_1^2 + C_2 z_2^2 + \dots + C_n z_n^2) = \frac{1}{2} \sum C_i z_i^2, \quad (14)$$

where z_i is the charge of the salts, and C_i is molar concentration. Higher ionic strength of the solution is obtained as the concentration of salts increases. Chen et al. demonstrated the influence of ionic strength on the adsorption of PR dye by tuning the concentration of NaCl [49]. The results showed a decreased adsorption capacity upon increasing the ionic strength because the adsorption of charged moieties competed with that of dye molecules or adsorbents in the solution. Similar results were also published [50–52].

Furthermore, the variation of pH value in the solution modifies the electrical double layer of the photocatalysts, which is composed of the charged surface of the photocatalyst and dye molecules in solution. Thus, a high adsorption capacity can be found when anionic or cationic dyes are respectively adsorbed on the photocatalyst surface at acidic or basic pH. The electrical double layer refers to the two layers between the photocatalyst and the bulk solution. Here, the region with dye molecules adsorbed onto the surface-charged photocatalyst is called the Stern layer. The surface-charged photocatalysts create an electrostatic field which affects the dye molecules in the solution, forming the first layer of the electrical double layer. The second diffusion layer is loosely associated with the photocatalyst and is composed of dye molecules that diffuse in the solution under the influence of electrostatic attraction. The electric potential at this plane is called the zeta potential, while the point of zero charge (pzc) forms where the zeta potential is 0. Depending on the solution pH, either positive or negative charges can be formed on a surface, since H^+ and OH^- are the charge-determining ions for most surfaces.

Amphoteric characteristics were observed in many photocatalyst materials, for example, $g\text{-C}_3\text{N}_4$ [53], TiO_2 [54], and most metal oxides. The formation of metal hydroxyl groups (M-OH) is attributed to the adsorption of H_2O molecules and dissociation of OH^- groups at surface metal sites. When the solution pH is higher than the pzc of photocatalysts, their surface is negatively charged; it is positively charged at pH value $<$ pzc of the photocatalysts. The equilibrium of amphoteric metal hydroxides under acidic and alkali conditions can be considered as



Therefore, at lower pH, protonation of the photocatalyst creates a surface with a positive charge, making the photocatalyst behave as a strong Lewis acid [55]. The anionic dye, with strongly ionized anionic groups, serves as a strong Lewis base and can be readily adsorbed on the positively charged photocatalyst surface, as shown in Figure 5a. This adsorption process is not favorable for negatively charged photocatalysts because of electrostatic repulsion [56], giving rise to negligible adsorption and a subsequent low degradation rate when $\text{pH} >$ pzc of the photocatalyst. Bourikas et al. reported that the adsorption of AO7 on the surface of TiO_2 cannot occur at a pH value higher than 7 [57] due to the electrostatic repulsion arising from the negative sulfonic group of the azo dye. Similar results were also observed for other anionic dye systems [58–60]. On the other hand, cationic dyes preferred to adsorb on the negatively charged photocatalysts in alkaline media. Bubacz et al. observed an increased photodegradation rate of MB on anatase TiO_2 with an increase in pH [61]. Fan et al. demonstrated that polyacrylonitrile fiber–hyperbranched polyethylenimine (PANF-g-HPEIs) activated with solutions at different pH may selectively adsorb cationic or anionic dyes [62]. Figure 5b,c show that PANF-g-HPEIs pre-treated with solution at pH = 5 can selectively adsorb the anionic MO dye from an MB/MO mixture, while PANF-g-HPEIs can selectively adsorb the cationic MB molecules after being pre-treated with solution at pH = 10.

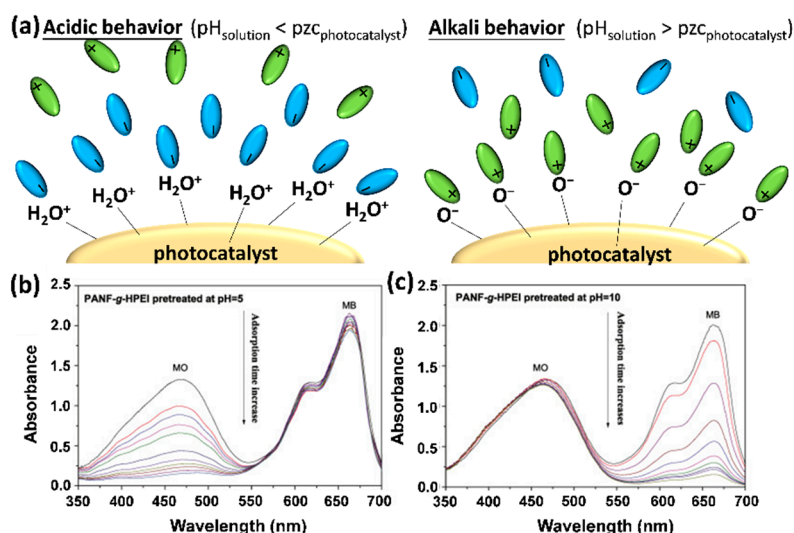


Figure 5. (a) Model of the absorption of cationic and anionic dye molecules on the photocatalyst surface under acidic and alkali conditions. Evolution of UV–visible absorption spectra of MO/MB mixed solution in the presence of PANF-g-HPEIs pre-treated at (b) pH = 5 and (c) pH = 10 (reproduced with permission from [62]. Copyright Elsevier Science Publishers, 2015).

Zhao et al. investigated the photodegradation efficiency for RhB-sensitized BiOCl nanostructures at pH 3.36 and pH 11.08 [63], as shown in Figure 6. Note that the self-photosensitization of cationic RhB adsorbed on negatively charged BiOCl nanostructures can degrade MO and RhB molecules at pH 3.36 and pH 11.08 (see Section 5.2). Both RhB and MO display efficient photodegradation within

5 min of visible irradiation at pH 3.36. However, the photodegradation of both RhB and MO was suddenly depressed in an alkali solution with pH 11.08, indicating the pH of solution strongly affects the electrical double layer, even though RhB can adsorb onto BiOCl nanostructures at both pH 3.36 and pH 11.08. In an acidic solution with pH 3.36, the presence of a high concentration of H^+ ions may push the cationic RhB molecules into the Stern layer, because of the electrostatic repulsion between H^+ ions and cationic RhB molecules in the diffusion layer, thus improving the electron transfer from RhB to BiOCl and the following photodegradation reaction. On the other hand, the electrostatic attraction of the increased OH^- ions to the cationic RhB molecules causes more RhB to stay in the diffusion layer in an alkali solution with pH 11.08, hindering the electron transfer from RhB to BiOCl and resulting in less efficient photodegradation.

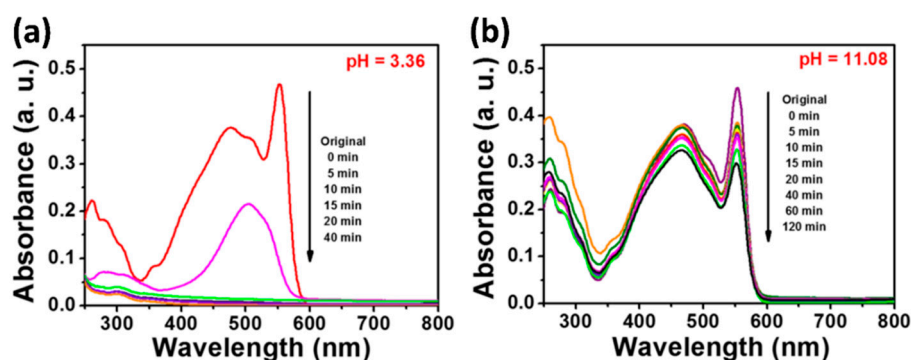


Figure 6. Photodegradation of MO on RhB-sensitized BiOCl hierarchical nanostructures at (a) pH = 3.36 and (b) pH = 11.08 (reproduced with permission from [63]. Copyright Royal Society of Chemistry, 2016).

Chen et al. further utilized the amphoteric properties of organosilica nanoparticles (OSNPs) to recover anionic PR molecules [49], based on the surface charge change of the OSNPs in acidic and alkali solutions. The morphology of the OSNP is shown in Figure 7a,b, which displays the apparent color of OSNP changing from white to pink. Interestingly, by controlling the pH of the solvent, PR was desorbed from the surface of the OSNPs in an NaOH solution, and the color of the OSNP returned to white, due to the negatively charged surface of the OSNP in NaOH solution. As can be seen in Figure 7c, the zeta potential of OSNPs returned to its initial value after PR desorption, which confirmed that OSNPs were stable during adsorption and desorption. Additionally, Figure 7d shows that adsorption/desorption tests of anionic PR molecules can be repeated for 10 cycles, further pointing out the high stability of OSNPs.

However, Kong et al. found a decline of the MB photodegradation reaction rates at high alkali pH [64], as shown in Figure 8. Although electrostatic attraction occurs between the cationic MB molecules and negatively charged surface of Ta-doped ZnO at alkali pH, the otherwise Coulombic repulsion of the negatively charged Ta-doped ZnO surface against the OH^- ions results in the breakage of hydroxylation of the ZnO surface. The Coulombic repulsion was reported for other cationic dyes (MB, RhB) at pH 9.5, which can reduce the number of $\cdot OH$ radicals and thereby decrease the photodegradation rate [65]. The steric structure of dyes also affects the adsorption process. Both MB and RhB are cationic dyes; however, research shows that MB exhibits a higher photodegradation rate than RhB, which can be attributed to the steric repulsion of the carboxylate anions in RhB which inhibits the extent of adsorption [65].

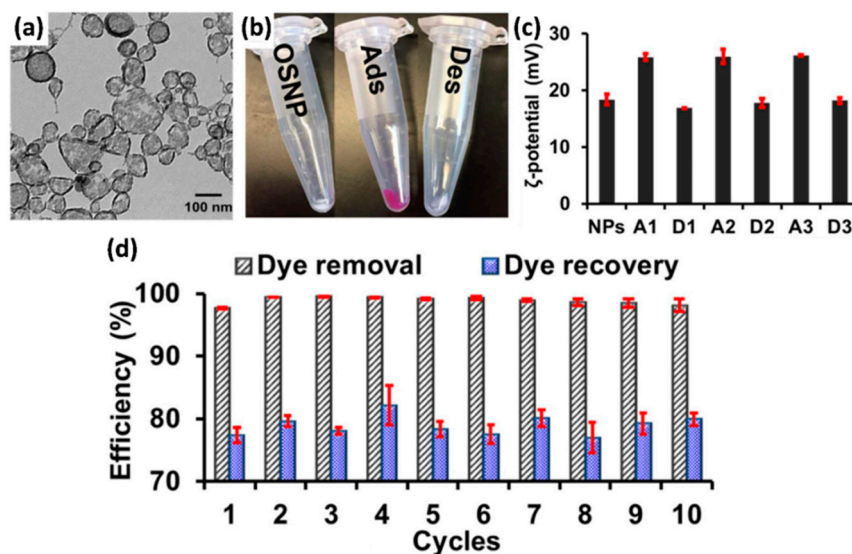


Figure 7. (a) TEM image for OSNPs. (b) Color change of OSNP after adsorption (Ads.) and desorption (Des.) of phenol red (PR). (c) Zeta potential of original OSNP and after three cycles of dye adsorption (A)/desorption (D). (d) PR adsorption/desorption recycle test for OSNP (reproduced with permission from [49]. Copyright American Chemical Society, 2017).

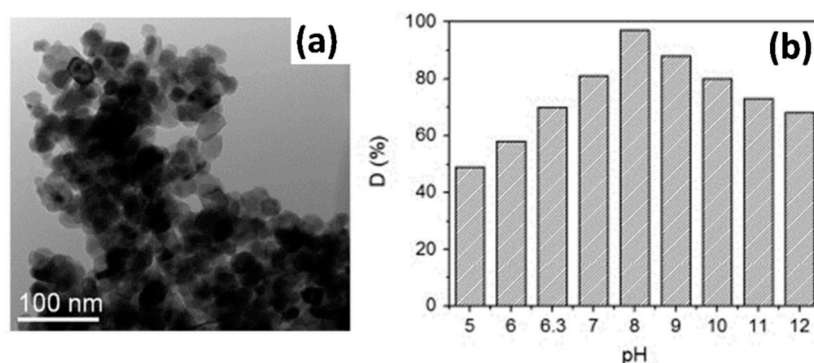


Figure 8. (a) TEM image and (b) pH effect on the photodegradation of MB over Ta-doped ZnO (reproduced with permission from [64]. Copyright Elsevier Science Publishers, 2010).

4.2. Operational Parameters

4.2.1. Initial Dye Concentration

The initial concentration of organic dyes strongly affects the photodegradation reaction. Saquib et al. demonstrated the photodegradation of gentian violet (also known as CV) with varying concentrations from 0.18 mM to 0.5 mM [66]. The photodegradation rate and TOC increased with the concentration of gentian violet up to 0.25 mM and then declined, as shown in Figure 9a. Kumar et al. reported that the degradation efficiency of VBB over TiO₂/polyaniline (PAni)/graphene oxide (GO) decreased with an increase in initial dye concentration [67], as shown in Figure 9b. This phenomenon was studied for other dye molecules, including the AR14/TiO₂ [3] and other systems [13,14,68,69]. Figure 9c shows the photodegradation of three different dye molecules (MG, MB, and RhB) over Fe₃O₄/reduced graphene oxide (rGO) photocatalysts [70]. The photodegradation efficiency also decreased with the increase in dye concentration.

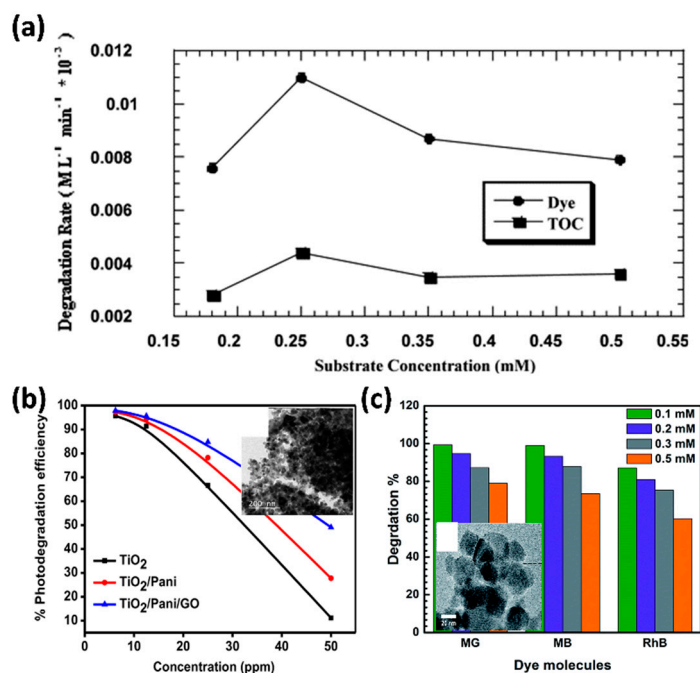


Figure 9. Effect of dye concentration for (a) gentian violet photodegradation on TiO_2 (reproduced with permission from [66]. Copyright Elsevier Science Publishers, 2003); (b) VBB photodegradation on TiO_2 , TiO_2/PAni , and $\text{TiO}_2/\text{PAni}/\text{GO}$ (reproduced with permission from [67]. Copyright John Wiley and Sons, 2018); (c) MG, MB, and RhB photodegradation on $\text{Fe}_3\text{O}_4/\text{rGO}$. (reproduced with permission from [70]. Copyright Royal Society of Chemistry, 2016). Insets of (b) and (c) are TEM images of $\text{TiO}_2/\text{PAni}/\text{GO}$ and $\text{Fe}_3\text{O}_4/\text{rGO}$, respectively.

The adsorption of dye molecules on the photocatalyst surface affects its ability of photon absorption and the subsequent generation of reactive radicals, posing a significant impact on the photodegradation rate. As the initial dye concentration increased, several monolayers of adsorbed dye formed, resulting in more adsorbed dye molecules available for photodegradation. Until reaching the critical level, constant reaction rate is obtained because the surface is completely covered. The photodegradation rate is, however, decreased with further increases in dye concentration. A high amount of adsorbed dye may have an inhibitive effect on the reactions between dye molecules and reactive radicals [71], since the excessive dye concentration may hinder light penetration to the solution [72] and fewer photons can reach the photocatalyst surface. Therefore, the generation of charge carriers and reactive radicals is simultaneously reduced, resulting in a decrease of photodegradation efficiency.

4.2.2. Light Intensity

It was shown that the photodegradation rate increases linearly with increasing light intensity at low light intensity. Figure 10a shows that the photodegradation of 2,4-dichlorophenoxyacetic acid (2,4-D) increased as light intensity increased from 100 to 600 lx [73], with the efficiency proportional to the light intensity. In Figure 10b, the photodegradation of benzene on nitrogen-doped TiO_2 was still enhanced by increasing light intensity, but the efficiency was nonlinearly increased [74]. With further increases to higher light intensity, the photodegradation rate became independent of light intensity. It is proposed that, at low light intensity, the separation of photoexcited electrons and holes competes with their recombination, thus impeding the generation of reactive radicals. The electron–hole generation becomes the predominant process as light intensity increases, resulting in a higher photodegradation rate. However, the total active sites for photodegradation remains constant and, therefore, the reaction rate shows a maximum value, even though the light intensity continues to increase [75].

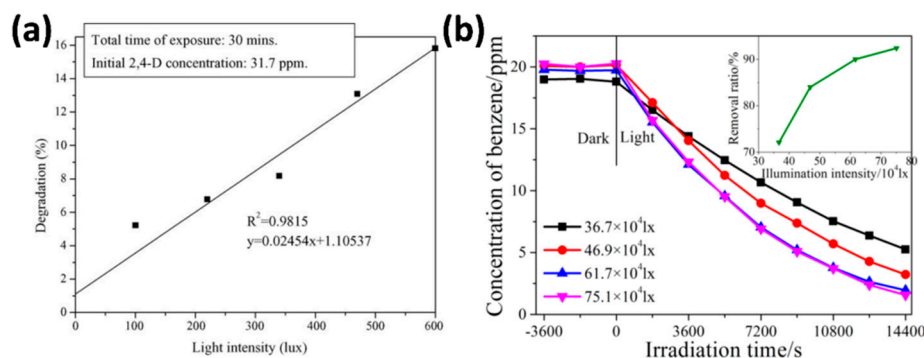


Figure 10. Effect of light intensity on the photodegradation of (a) 2,4-D with low light intensity (100–600 lx) (reproduced with permission from [73]. Copyright Elsevier Science Publishers, 2005), and (b) benzene with high light intensity (36.7×10^4 – 75.1×10^4 lx) (reproduced with permission from [74]. Copyright MDPI, 2018).

4.2.3. Reaction Temperature

Not only do initial dye concentration and light intensity possess optimal conditions, but an optimal temperature range also exists for photodegradation. Low temperature favors the adsorption of the reactant, which is a spontaneous exothermic process, whereas the apparent activation energy increases as the temperature decreases close to 0 °C. Low temperature also favors the adsorption of the final product, albeit while decreasing the number of active sites. Therefore, compared to photodegradation and the adsorption of reactants, the slower desorption of product inhibits the reaction and serves as the rate-limiting step under low reaction temperatures. In contrast, when the temperature increases up to the boiling point of the solvent (water for most of the cases), the exothermic adsorption of reactants becomes disfavored, thus limiting the photodegradation reaction [76]. Charge-carrier recombination is also substantially promoted [77] as the reaction temperature exceeds 80 °C. At higher temperatures, the enhanced kinetic energy of dye molecules might allow them escape from the photocatalyst surface [78], leading to decreased photodegradation efficiency. Thus, the adsorption of dye molecules becomes the limiting step at high temperatures. As a result, reaction temperatures between 20 and 80 °C [15] are considered as the desired temperature for the effective photodegradation of dye molecules.

4.3. Intrinsic Properties of Photocatalysts

The photodegradation efficiency can be enhanced by increasing the photocatalyst amount, which is a feature of heterogeneous photocatalysis. The increased photocatalyst amount provides more active sites for the discoloration of dye solution. However, beyond a certain amount, the reaction solution turns into turbid and is subjected to limited light penetration to the photocatalyst surface, leading to the inhibition of the photodegradation reaction.

In addition, the intrinsic properties of the photocatalyst, such as light absorption range, redox potential, charge separation efficiency, and stability, strongly affect the photodegradation activity. The fast charge recombination of a single-component material limits its photodegradation efficiency. Additionally, the single-component photocatalyst cannot simultaneously satisfy the requirement of large redox potential and wide light absorption. To improve the photocatalytic efficiency, a variety of studies were devoted to exploring new heterostructure systems and using them in the photodegradation reaction. Typical strategies include element doping, metal decoration, and semiconductor modification (type II and Z-scheme heterostructures), which can broaden the light absorption range to enhance the light utilization and inhibit charge recombination. Among the aforementioned factors, charge-carrier dynamics are crucial for determining the overall photocatalytic efficiency. It is, thus, of great importance to study the underlying charge-carrier dynamics in semiconductor photocatalysts. Time-resolved PL (TRPL) techniques were demonstrated to be a powerful tool to observe the charge transfer processes of semiconductor heterostructures. In this

section, the implication of charge-carrier dynamics in the photodegradation efficiency for the three most relevant heterostructure systems, i.e., metal–semiconductor, type II semiconductor–semiconductor, and Z-scheme semiconductor–metal–semiconductor heterostructures, is discussed.

4.3.1. Modification with Metals

Au–CdS metal–semiconductor nanocrystals were demonstrated to photodegrade RhB molecules [79]. Using TRPL to study the photoexcited charge transfer kinetics, Figure 11a,b display the TRPL spectra for two Au–CdS nanocrystals with different shell thicknesses (14.0 nm and 18.6 nm). Compared with their CdS counterpart, obtained by etching Au cores, a fast decay was found in Au–CdS samples, indicating electron transfer from CdS to Au. This difference became more noticeable for Au–CdS with shell thickness increasing to 18.6 nm, suggesting much more pronounced electronic interaction between CdS and Au. By further analysis with biexponential kinetics, the interfacial charge transfer rate constant (k_{ct}) was estimated. In addition, the photodegradation rate constant (k_{RhB}) changed with CdS thickness in the core–shell nanocrystals, as shown in Figure 11c. It was enhanced with increasing shell thickness due to the raised ratio of CdS to Au, which led to greater light absorption and, thus, generation of more charge carriers. The correlation among k_{RhB} , k_{ct} , and CdS shell thickness is shown in Figure 11d. The change in k_{ct} with CdS shell thickness was consistent with the trend of k_{RhB} , revealing that efficient charge separation can provide a hole-enriched CdS shell for the photodegradation reaction and further enhance the photodegradation efficiency.

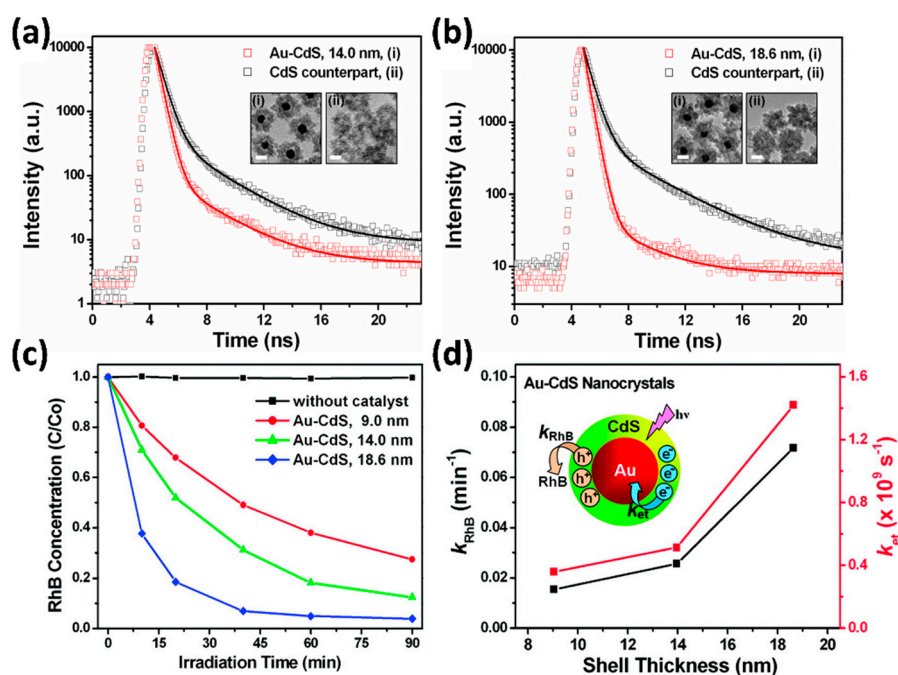


Figure 11. TRPL spectra (dots) and fitting results (solid curves) of Au–CdS and pure CdS nanocrystals with shell thicknesses of (a) 14.0 nm and (b) 18.6 nm (inset shows the corresponding TEM images, with scale bar of 20 nm). (c) RhB photodegradation under visible irradiation and (d) correlations of k_{ct} and k_{RhB} for Au–CdS nanocrystals with different shell thicknesses (reproduced with permission from [79]. Copyright American Chemical Society, 2010).

Moreover, the metal content and composition were tuned in a metal (Ag, Au, Pd)-decorated ZnO system for photodegradation of MB in ethanol [80]. The morphology of ZnO–Au with different Au contents is shown in Figure 12a. The Au content is obviously increasing and was measured to be 0.6 at.%, 1.0 at.%, 1.3 at.%, 2.0 at.%, and 2.3 at.%. As shown in Figure 12b,c, an optimal Au content for the photodegradation reaction was found, as excess metal loading for metal–semiconductor heterostructures may compromise the effectiveness of the overall charge separation. Figure 12d also

indicates that the photodegradation rate of ZnO–Pd was higher than that of ZnO–Au, while ZnO–Ag was the worst. This is due to the most positive Fermi level potential of Pd. Larger differences between the CB of ZnO and the Fermi level (E_F) of the metal result in stronger driving forces for interfacial charge transfer, giving rise to the most efficient charge separation for ZnO–Pd and the most effective photodegradation of MB molecules.

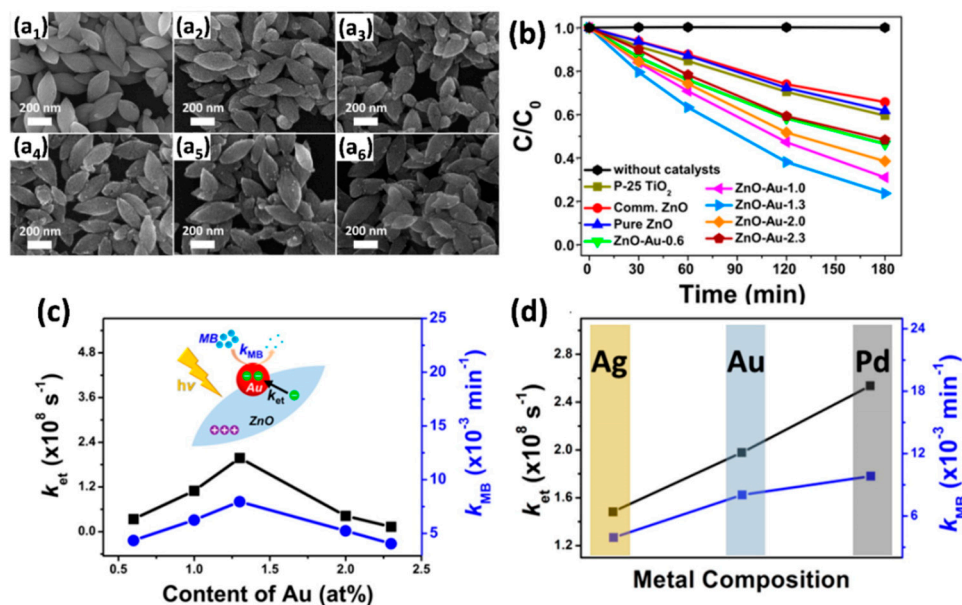


Figure 12. SEM observations for (a₁) pure ZnO and (a₂–a₆) ZnO–Au nanocrystals with increasing Au content from 0.1 at.% to 2.3 at.%. (b) Photodegradation of MB on relevant photocatalysts under UV irradiation. (c) Correlations of k_{et} and k_{MB} for ZnO–Au with different Au content and for (d) ZnO–metal (Ag, Au, Pd) with different metal content (reproduced with permission from [80]. Copyright American Chemical Society, 2016).

4.3.2. Modification with Semiconductors

CdS–CdSnO₃ type-II heterostructures were also employed to investigate the effect of CdSnO₃ content for the photodegradation of RhB [81]. Figure 13a shows the direct contact of CdS and CdSnO₃, and the content of CdSnO₃ was precisely controlled. The surface-decorated CdSnO₃ acts as an efficient electron scavenger for CdS because of its lower CB level (+0.9 V vs. NHE) than the CB level of CdS (−0.5 V vs. NHE), giving rise to the fast PL decay of CdS–CdSnO₃, as shown in the TRPL analysis in Figure 13b. As a result, the photoexcited electrons of CdS nanowires preferentially transferred to CdSnO₃ nanocrystals, leaving photoexcited holes in the CdS domain to react with RhB molecules. As shown in Figure 13c, the photodegradation rate was enhanced with CdSnO₃ content increasing from 1.25 at.% to 2.5 at.%, and then depressed with further increases in CdSnO₃ content. This observation was in accordance with their interfacial charge transfer kinetics, indicating that an excess amount of CdSnO₃ would reduce the overall charge separation efficiency and result in the depressed photocatalytic efficiency, as shown in Figure 13d. The amounts affecting the subsequent photodegradation performance were also proposed in ZnSe–ZnO [82], In₂O₃–TiO₂–Pt [83], and Cu₂O–rGO [84] heterostructures. These observations indicate that the interfacial charge transfer kinetics of the photocatalysts play an important role for the photodegradation of dye molecules. Moreover, the composition and facet effects of heterostructure systems such as TiO₂–Au@Cu₇S₄ [85] and ZnS–Cu₂O [86] also influence the photodegradation efficiency.

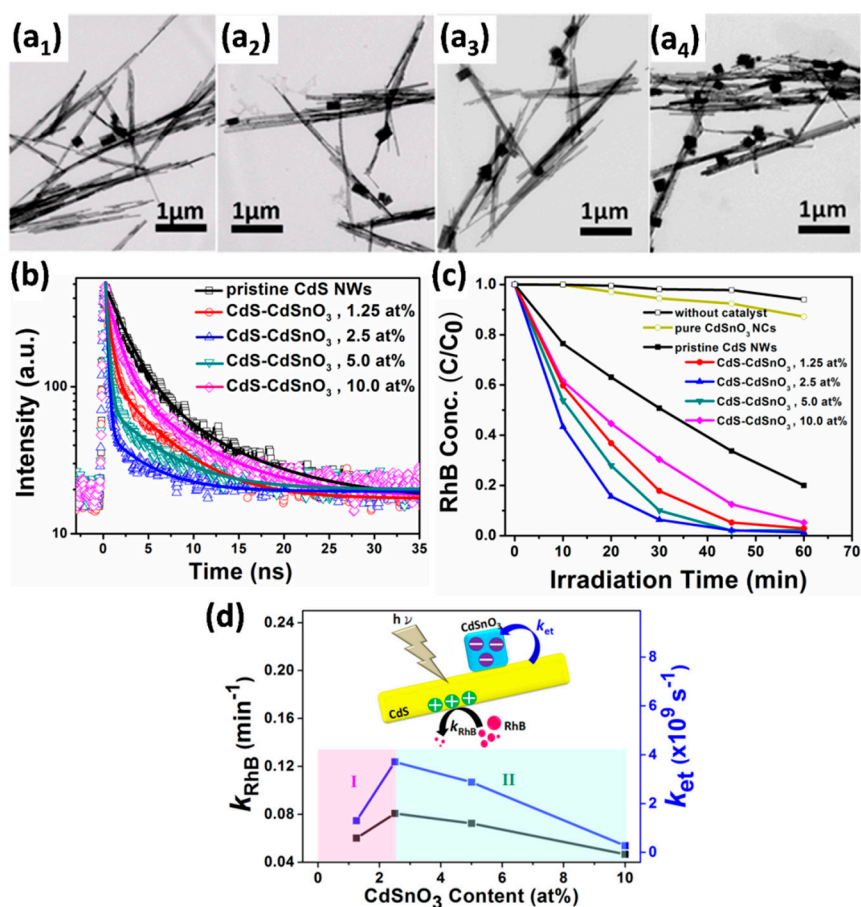


Figure 13. (a1–a4) TEM images for CdS–CdSnO₃ with increasing CdSnO₃ content from 1.25 at.% to 10.0 at.%. (b) TRPL analysis. (c) RhB photodegradation under visible irradiation and (d) correlations of k_{et} and k_{RhB} for CdS–CdSnO₃ with increasing CdSnO₃ content (reproduced with permission from [81]. Copyright Elsevier Science Publishers, 2010).

4.3.3. Modification with Metals and Semiconductors

Na_{2-x}Ti₃O₇–Au–Cu₂O Z-scheme heterostructure nanobelts (denoted as ST–Au–Cu₂O NBs) were demonstrated to photodegrade MB molecules [87]. Figure 14a,b display the successful decoration of Au nanoparticles on ST and the further growth of Cu₂O on Au surface. By decreasing the volume of the Cu²⁺–citrate precursor, the shell thickness of the grown Cu₂O can be tuned from 1.4 nm and 1.2 nm to 1.1 nm, resulting in the modulation of interfacial charge transfer dynamics and, thus, the enhancement of photodegradation efficiency. As shown in Figure 14c, the ST–Au–Cu₂O Z-scheme NBs showed higher photodegradation efficiency than ST–Au and ST–Cu₂O type-II NBs, illustrating the superiority of Z-scheme heterostructures in photodegradation applications. Meanwhile, the highest photodegradation efficiency was achieved for ST–Au–Cu₂O prepared with 50 μL of Cu²⁺–citrate, which can be attributed to the most efficient charge transfer dynamics at the Cu₂O thickness of 1.1 nm. As Figure 14d presents, the electron-scavenging rate constant (k_{es}) for ST–Au–Cu₂O was enhanced with decrease in Cu₂O shell thickness, which can be ascribed to the quantum size effect of Cu₂O. Since decreasing Cu₂O shell simultaneously expanded the bandgap of Cu₂O, its CB and VB respectively shifted toward higher and lower potential, giving a larger driving force of interfacial electron transfer for ST–Au–Cu₂O and thereby improving the photodegradation efficiency.

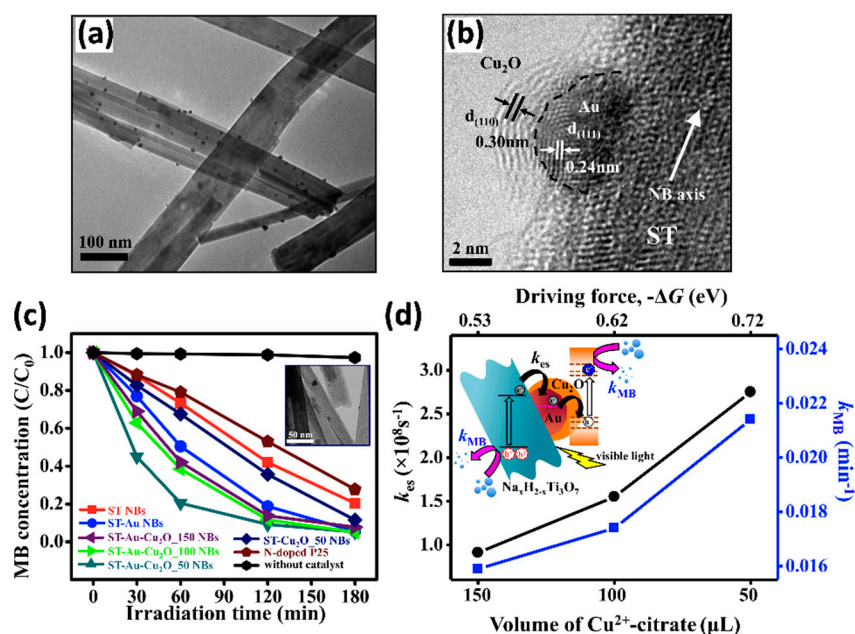


Figure 14. TEM images of (a) ST-Au and (b) ST-Au-Cu₂ONBs. (c) Photodegradation of MB on relevant photocatalysts under visible irradiation (inset shows the TEM image of ST-Cu₂O NBs). (d) Correlations of k_{es} and k_{MB} with the amount of Cu²⁺-citrate and the driving force ($-\Delta G$) of interfacial electron transfer for ST-Au-Cu₂O (reproduced with permission from [87]. Copyright Elsevier Science Publishers, 2015).

5. Mechanism for Photodegradation of Dye

Figure 15 displays the redox potentials for the reactive species and the band structures of common photocatalysts, along with the lowest unoccupied molecular orbital (LUMO) and highest occupied molecular orbital (HOMO) levels of five representative dye molecules. Based on their band positions, the generation of reactive species in semiconductor photocatalysts can directly degrade dye molecules (see Section 5.1). Alternatively, the self-photosensitization of dye may occur to improve the generation of reactive species when the CB of photocatalysts is more negative than the LUMO level of dye molecules (see Section 5.2), finally dissociating the dye molecules.

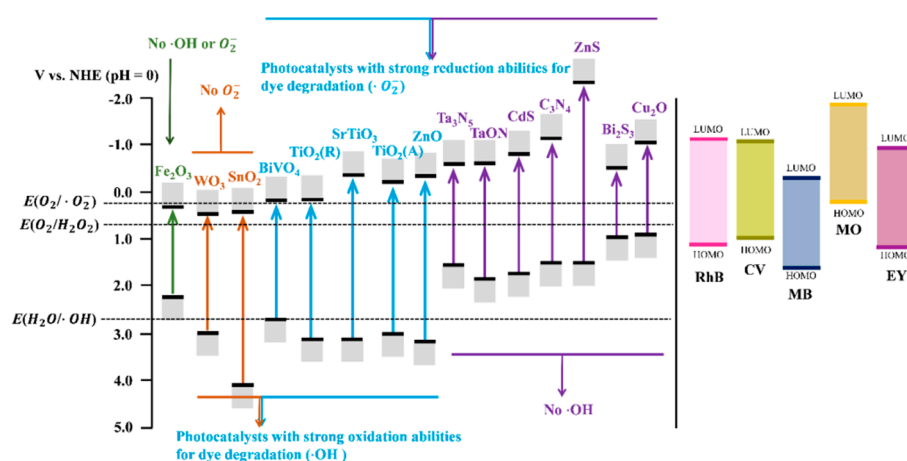


Figure 15. Scheme for the band structures of common photocatalysts, and potentials of the radical generation and HOMO and LUMO levels of five representative dye molecules.

5.1. Direct Photodegradation Process

In principle, the direct photodegradation of dye molecules involves the excitation of semiconductor photocatalysts under light irradiation, leading to the scavenging of photoexcited electrons by dissolved

O₂ in the solution, as the CB of the photocatalyst is more negative than the reduction potential $E(\text{O}_2/\cdot\text{O}_2^-)$. The $\cdot\text{O}_2^-$ anion and H₂O₂ are, thus, formed. H₂O₂ can further transform into $\cdot\text{OH}$. Meanwhile, the photoexcited holes can oxidize the adsorbed water to generate $\cdot\text{OH}$, as the VB of photocatalysts are more positive than the oxidation potential $E(\text{H}_2\text{O}/\cdot\text{OH})$. These highly reactive $\cdot\text{O}_2^-$ and $\cdot\text{OH}$ can oxidize or degrade the adsorbed dye molecules. In addition, the photoexcited electrons and holes which are essentially active may also attack the dye molecules to complete the photodegradation process.

To clarify the major contributor in the photodegradation reaction, several studies investigated the change of the photodegradation rate in the presence of different scavengers, as listed in Table 2. Pu et al. developed a Cu₂O-rGO system (Figure 16a) and explored the photodegradation mechanism of MO, with TBA used as the $\cdot\text{OH}$ scavenger [84]. Figure 16b shows various control experiments for the photodegradation of MO. No obvious change on MO photodegradation was found with the addition of TBA, indicating that the photoexcited holes of Cu₂O and the subsequent $\cdot\text{OH}$ radicals were minor factors. Furthermore, the photodegradation reaction was performed with purging using O₂ and N₂. The MO photodegradation was abated under an N₂ purge, whereas the photodegradation rate was slightly enhanced under O₂ purging, confirming that dissolved O₂ in the solution played a crucial role for the MO photodegradation. Figure 16c shows the pathway for the MO photodegradation in the Cu₂O/rGO system. Upon light irradiation, the photoexcited electrons transfer to the E_F of rGO, and the generation of $\cdot\text{O}_2^-$ occurs, degrading the MO molecules. As demonstrated by Zhao's group, $\cdot\text{O}_2^-$ is one of the main active species for MO photodegradation [88], which was also confirmed by the seriously depressed photodegradation of MO (to almost no activity) in the absence of O₂. Li et al. also confirmed that photoexcited holes are a minor active species and the dissolved O₂ dominates the MO photodegradation on g-C₃N₄ photocatalyst [89] because the formation of $\cdot\text{O}_2^-$ is affected by direct reduction of O₂. The presence of O₂ also determines the production of $\cdot\text{OH}$ via multistep reduction of O₂.

Table 2. Common scavengers used for active species trapping experiments.

Type	Sacrifice Reagent	Abbreviation
Electron scavenger	AgNO ₃	-
	CCl ₄	-
	K ₂ Cr ₂ O ₇	-
Hole scavenger	KI	-
	Ethylenediaminetetraacetic acid	EDTA, EDTA-2Na
	Tri-ethanolamine	TEOA
	Ammonium oxalate	AO
	Sodium oxalate (Na ₂ C ₂ O ₄)	-
	Methanol	-
$\cdot\text{OH}$ scavenger	Ascorbic acid	AA
	<i>tert</i> -Butyl alcohol	TBA, t-BuOH
	2-Propanol	IPA
$\cdot\text{O}_2^-$ scavenger	Benzoquinone	BQ
	Acrylamide	AC
	Superoxide dismutase	SOD

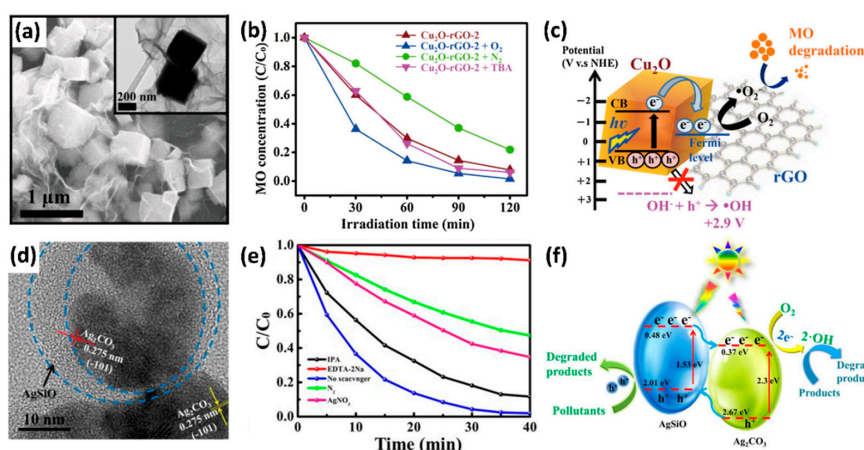


Figure 16. (a) SEM and TEM (inset) observations and (b) MO photodegradation over $\text{Cu}_2\text{O-rGO}$ under different experimental conditions. (c) Schematic illustration of the band structure and relevant redox potentials for $\text{Cu}_2\text{O-rGO}$ (reproduced with permission from [84]. Copyright Elsevier Science Publishers, 2015). (d) High-resolution (HR) TEM image of $\text{AgSiO/Ag}_2\text{CO}_3$. (e) MB photodegradation under visible irradiation in the presence of scavengers and (f) proposed mechanisms of photodegradation pathways of MB on $\text{AgSiO/Ag}_2\text{CO}_3$ (reproduced with permission from [90]. Copyright Nature Publishing Group, 2017).

Cao et al. proposed that the photodegradation of MB on $\text{AgSiO/Ag}_2\text{CO}_3$ photocatalysts in water was dominated by $\cdot\text{O}_2^-$ and photoexcited holes [90]. Figure 16d shows the morphology of $\text{AgSiO/Ag}_2\text{CO}_3$ photocatalysts. With addition of IPA, the photodegradation rate slightly decreased, suggesting $\cdot\text{OH}$ was not the main active species (Figure 16e). Meanwhile, the addition of EDTA-2Na and N_2 purging resulted in a significant decrease of photodegradation efficiency, indicating the important roles of $\cdot\text{O}_2^-$ and photoexcited holes in the photodegradation process of MB. The possible photodegradation pathway is displayed in Figure 16f. This photodegradation pathway can be supported by adding AgNO_3 into the reaction solution. The suppression of the photodegradation rate in the presence of AgNO_3 is due to the decreased generation of $\cdot\text{O}_2^-$ from photoexcited electrons. This outcome was also consistent with the $\text{g-C}_3\text{N}_4$ [91], ZnO/graphene [92], and $\text{C}_3\text{N}_4\text{-BiVO}_4$ [93] systems for the photodegradation of MB. The aforementioned scavenger experiments revealed that major contributors for each dye molecule might be different. Table 3 specifies the dominating active species for other commonly reported dye molecules.

Table 3. Active species for photodegradation of commonly reported dyes molecules.

Class	Dye	Active Species	Photocatalysts
Cationic dye	RhB	H^+	$\text{g-C}_3\text{N}_4$ [89]
		H^+	$\text{Ag/Ag}_3\text{PO}_4$ [94]
		$\cdot\text{O}_2^-/\text{H}^+$	$\text{BiVO}_4/\text{TiO}_2$ [95]
		$\cdot\text{O}_2^-/\text{H}^+$	BiOI/C [96]
	MB	H^+ (major), $\cdot\text{O}_2^-$ (minor)	$\text{CoFe}_2\text{O}_4/\text{BiO}(\text{Cl, Br, I})$ [34]
		$\cdot\text{O}_2^-/\text{H}^+$	$\text{g-C}_3\text{N}_4$ [91]
		$\cdot\text{O}_2^-/\text{H}^+$	ZnO/graphene [92]
Anionic dye	CV	$\cdot\text{O}_2^-$	$\text{C}_3\text{N}_4\text{-BiVO}_4$ [93]
		$\cdot\text{O}_2^-/\text{H}^+$	$\text{AgSiO/Ag}_2\text{CO}_3$ [90]
		$\cdot\text{O}_2^-$	$\text{AgSiO/Ag}_2\text{CO}_3$ [90]
	MG	$\cdot\text{O}_2^-$ (major), $\text{h}^+/\cdot\text{OH}$ (minor)	$\text{BiO}_x\text{Cl}_y/\text{BiO}_m\text{I}_n$ [97]
		$\cdot\text{O}_2^-$ (major), $\text{h}^+/\cdot\text{OH}$ (minor)	$\text{BiO}_x\text{I}_y/\text{GO}$ [98]
		$\cdot\text{O}_2^-/\text{h}^+$ (major), $\cdot\text{OH}$ (minor)	BaFe_2O_4 [99]
Rh6G	$\text{H}^+/\cdot\text{OH}/\cdot\text{O}_2^-$	CuFe_2O_4 [100]	
	$\cdot\text{OH}/\text{e}^-/\text{H}^+$ (major), $\cdot\text{O}_2^-$ (minor)	$\text{Fe}_3\text{O}_4/\text{TiO}_2/\text{CuO}$ [101]	
	$\cdot\text{OH}/\text{e}^-/\text{H}^+$ (major), $\cdot\text{O}_2^-$ (minor)	$\text{Ni-Bi}_2\text{Se}_3$ [102]	
Neutral dye	Curcumin	H^+ (major), $\cdot\text{OH}/\cdot\text{O}_2^-$ (minor)	$\text{Curcumin/Bi}_{0.5}\text{Na}_{0.5}\text{TiO}_3$ [103]
		$\cdot\text{O}_2^-$	Zn/Y [104]
Metal-organic framework	Quantum dot	$\text{H}^+/\cdot\text{O}_2^-$	Quantum dot/Eu-metal organic framework [105]

Table 3. Cont.

Class	Dye	Active Species	Photocatalysts
Anionic dye	MO	$\cdot\text{O}_2^-$	Cu ₂ O-rGO [84]
		$\cdot\text{O}_2^-$	2,9,16,23-tetracarboxyl phthalocyanine/amorphous TiO ₂ [88]
		$\cdot\text{O}_2^-$ (major) H ⁺ (minor)	g-C ₃ N ₄ [89]
	AO7	H ⁺ /OH	TiO ₂ [106]
		h ⁺	Ag/AgBr/SiO ₂ -coated Fe ₃ O ₄ [107]
	CR	$\cdot\text{OH}$	ZrO ₂ [108]
		H ⁺ /OH H ⁺ (major), $\cdot\text{OH}$ (minor)	CuS-Bi ₂ Cu _x W _{1-x} O _{6-2x} [109] SnO ₂ [110]
	ARS	$\cdot\text{OH}/e^-/\text{H}^+$	ZnS/carbon quantum dots [111]
AV7	$\cdot\text{O}_2^-/\text{H}^+/\text{OH}$	CdS/Ta ₂ O ₅ [112]	
RB5	H ⁺	SrTiO ₃ /CeO ₂ [113]	

5.2. Sensitization-Mediated Degradation Process

When the photon energy is not high enough to excite photocatalysts to generate reactive charge carriers and radicals, the photodegradation might occur via photosensitization process. Under visible light illumination, a dye molecule can be excited to its excited state (LUMO level), producing abundant excited electrons at the LUMO level. Provided that the LUMO of the dyes is more negative than the CB of photocatalysts, these photoexcited electrons can then transfer from the dye molecules to the photocatalysts, facilitating the generation of reactive species for commencing photodegradation. This process is known as the photosensitization pathway. The LUMO levels for five representative dye molecules in comparison with the CB levels of common photocatalysts are illustrated in Figure 15, from which one can tell whether or not the photosensitization can occur. Zhao et al. demonstrated the self-photosensitization process of RhB and MO over BiOCl hierarchical nanostructures [63], as shown in Figure 17a. Note that the as-synthesized BiOCl exhibits a negatively charged surface in the pH range from 2 to 11, suggesting the as-synthesized BiOCl can selectively adsorb cationic RhB in RhB/MO mixtures. As shown in Figure 17b,c, RhB showed almost 40% adsorption prior to the light irradiation, while MO showed a negligible adsorption. Upon visible light irradiation, although BiOCl nanostructures cannot be excited with visible light since the bandgap of BiOCl is approximately 3.3 eV, the RhB dye was completely degraded within 15 min, whereas no photodegradation was found for the MO/BiOCl system (Figure 17d). The RhB photodegradation was attributed to the self-photosensitization of RhB, in which the photoexcited electrons are injected from the LUMO level of RhB to the CB of the BiOCl nanostructures. The electrons on the BiOCl nanostructures can subsequently reduce O₂ to $\cdot\text{O}_2^-$ radicals, which further degrades the RhB molecules. The self-photosensitization of MO should also be able to degrade the MO molecules; however, its poor adsorption capacity inhibits the electron transfer from the excited MO to the CB of BiOCl. Therefore, BiOCl nanostructures exhibited poor MO photodegradation efficiency. The self-photosensitization of the RhB/BiOCl system can be further applied to the photodegradation of MO dye molecules, as shown in Figure 17e. Compared to the extremely low MO photodegradation efficiency in the MO/BiOCl system, apparently, the MO photodegradation efficiency was significantly enhanced in the MO/RhB/BiOCl system, indicating that MO photodegradation is mediated by RhB via a photosensitization pathway. Moreover, RhB still demonstrated a higher photodegradation efficiency in the MO/RhB/BiOCl system. This photodegradation of dye molecules via the photosensitization process was reported in the cationic new fuchsin/graphene quantum dots [114], RhB/Zn-doped BiOBr [115], MB and MO/Eu³⁺-doped ZnO [116], and RhB/Nb₂O₅ [117] systems.

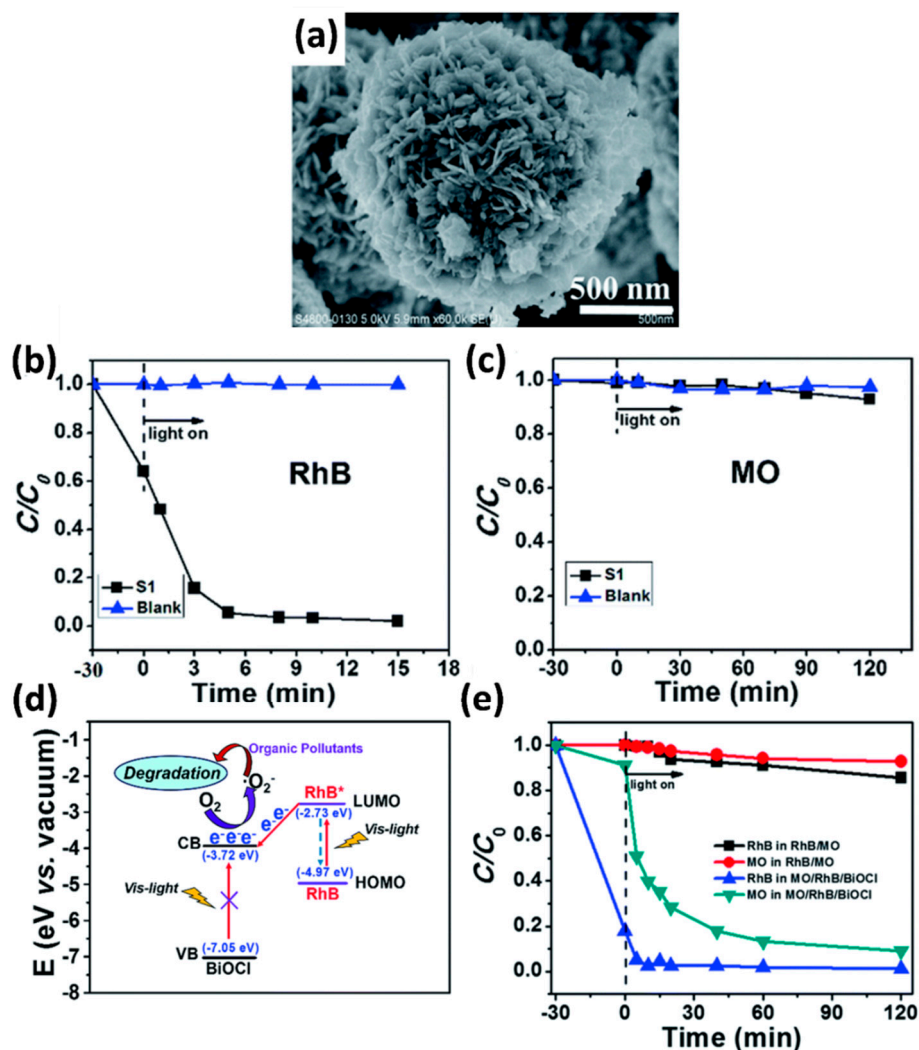


Figure 17. (a) SEM image of BiOCl and the results of (b) RhB and (c) MO photodegradation under visible irradiation. (d) Proposed mechanism for the enhanced MO photodegradation on RhB/BiOCl under visible irradiation. (e) Photodegradation of RhB and MO on RhB/BiOCl (reproduced with permission from [63]. Copyright Royal Society of Chemistry, 2016).

6. Summary and Outlook

Most dyes have either a positive or a negative charge upon dissociation in aqueous solutions, characteristic of cationic and anionic dyes, respectively. The pH of the solution modifies the electrical double layer of the photocatalyst, affecting the interaction between dye molecules and photocatalysts, the charge transfer for the self-photosensitization of dyes, and the subsequent decoloration efficiency, as highlighted in this review. The optimization of other operational factors (i.e., initial dye concentration, light intensity, reaction temperature) and charge-carrier properties of heterostructure photocatalysts can establish the most efficient photodegradation system. In addition, research on the reactive species, as well as the photosensitization pathway of dye molecules for photodegradation, is helpful to clarify the overall decoloration mechanism, which is beneficial for further application to the degradation of multicomponent industrial wastewaters. With strong progress in photocatalytic techniques, more in-depth characterization and modeling of the photodegradation, and even mineralization processes for multicomponent dyes in practical applications will be possible in the near future. Clearly, many questions still remain unanswered or are poorly addressed, which are briefly outlined below.

Unlike other heterogeneous photocatalysis, such as photoelectrochemical water splitting and CO₂ reduction in which the solar-to-hydrogen (STH) and AQY are introduced to determine the

photocatalytic efficiency for comparison, a quantitative comparison with AQY is relatively unexplored for photodegradation reactions. The introduction of AQY into the photodegradation reaction provides helpful information to understand the efficiency of semiconductor photocatalysts. However, for visible-light-responsive photocatalysts, the feasible determination of photodegradation efficiency is especially challenging due to the relatively high photoabsorption coefficient of dye molecules, as well as the complicated mechanism of dye degradation [118].

Another major concern in reactions involving self-photosensitization of dye molecules is the interactions between photocatalysts and multiple types of dye molecules, which are not always clear. Limited studies described the underlying interactions and mechanisms. By using self-photosensitization of dye molecules, both cationic and anionic dyes can be simultaneously decomposed, which has the potential to degrade multicomponent dyes in real wastewater systems. However, for multicomponent dye systems, the quantification of efficiency for each individual dye molecule is difficult to determine with simple spectrophotometric methods especially when their absorption spectra overlap. The development of a new method to easily and reliably obtain quantitative detection of dye molecules is necessary for accurate estimation.

Author Contributions: Conceptualization, Y.-H.C.; investigation, Y.-H.C., T.-F.M.C., C.-Y.C., M.S., and Y.-J.H.; writing—original draft preparation, Y.-H.C.; writing—review and editing, Y.-J.H.

Funding: This work was financially supported by the JST CREST of Japan (Grant Number JPMJCR1433), the Ministry of Science and Technology (MOST) of Taiwan (grant No. MOST 107-2113-M-009-004 and MOST108-3017-F-009-004) and the Center for Emergent Functional Matter Science of National Chiao Tung University from the Featured Areas Research Center Program within the framework of the Higher Education Sprout Project by the Ministry of Education in Taiwan.

Conflicts of Interest: The authors declare no conflict of interest.

References

1. Brown, M.A.; De Vito, S.C. Predicting azo dye toxicity. *Crit. Rev. Environ. Sci. Technol.* **1993**, *23*, 249–324. [[CrossRef](#)]
2. Chen, S.; Zhang, J.; Zhang, C.; Yue, Q.; Li, Y.; Li, C. Equilibrium and kinetic studies of methyl orange and methyl violet adsorption on activated carbon derived from *Phragmites australis*. *Desalination* **2010**, *252*, 149–156. [[CrossRef](#)]
3. Daneshvar, N.; Salari, D.; Khataee, A.R. Photocatalytic degradation of azo dye acid red 14 in water: Investigation of the effect of operational parameters. *J. Photochem. Photobiol. A Chem.* **2003**, *157*, 111–116. [[CrossRef](#)]
4. Ledakowicz, S.; Gonera, M. Optimisation of oxidants dose for combined chemical and biological treatment of textile wastewater. *Water Res.* **1999**, *33*, 2511–2516. [[CrossRef](#)]
5. Grzechulska, J.; Morawski, A.W. Photocatalytic decomposition of azo-dye acid black 1 in water over modified titanium dioxide. *Appl. Catal. B Environ.* **2002**, *36*, 45–51. [[CrossRef](#)]
6. Haque, E.; Jun, J.W.; Jhung, S.H. Adsorptive removal of methyl orange and methylene blue from aqueous solution with a metal-organic framework material, iron terephthalate (MOF-235). *J. Hazard. Mater.* **2011**, *185*, 507–511. [[CrossRef](#)] [[PubMed](#)]
7. Shi, B.; Li, G.; Wang, D.; Feng, C.; Tang, H. Removal of direct dyes by coagulation: The performance of preformed polymeric aluminum species. *J. Hazard. Mater.* **2007**, *143*, 567–574. [[CrossRef](#)]
8. Galindo, C.; Jacques, P.; Kalt, A. Photooxidation of the phenylazonaphthol AO20 on TiO₂: Kinetic and mechanistic investigations. *Chemosphere* **2001**, *45*, 997–1005. [[CrossRef](#)]
9. Aleboye, A.; Aleboye, H.; Moussa, Y. “Critical” effect of hydrogen peroxide in photochemical oxidative decolorization of dyes: Acid Orange 8, Acid Blue 74 and Methyl Orange. *Dyes Pigments* **2003**, *57*, 67–75. [[CrossRef](#)]
10. Ayodhya, D.; Veerabhadram, G. A review on recent advances in photodegradation of dyes using doped and heterojunction based semiconductor metal sulfide nanostructures for environmental protection. *Mater. Today Energy* **2018**, *9*, 83–113. [[CrossRef](#)]

11. Aramendía, M.A.; Marinas, A.; Marinas, J.M.; Moreno, J.M.; Urbano, F.J. Photocatalytic degradation of herbicide fluroxypyr in aqueous suspension of TiO₂. *Catal. Today* **2005**, *101*, 187–193. [[CrossRef](#)]
12. Lee, Y.Y.; Moon, J.H.; Choi, Y.S.; Park, G.O.; Jin, M.; Jin, L.Y.; Li, D.; Lee, J.Y.; Son, S.U.; Kim, J.M. Visible-Light Driven Photocatalytic Degradation of Organic Dyes over Ordered Mesoporous Cd_xZn_{1-x}S Materials. *J. Phys. Chem. C* **2017**, *121*, 5137–5144. [[CrossRef](#)]
13. Shahwan, T.; Abu Sirriah, S.; Nairat, M.; Boyacı, E.; Eroğlu, A.E.; Scott, T.B.; Hallam, K.R. Green synthesis of iron nanoparticles and their application as a Fenton-like catalyst for the degradation of aqueous cationic and anionic dyes. *Chem. Eng. J.* **2011**, *172*, 258–266. [[CrossRef](#)]
14. Neppolian, B.; Choi, H.C.; Sakthivel, S.; Arabindoo, B.; Murugesan, V. Solar/UV-induced photocatalytic degradation of three commercial textile dyes. *J. Hazard. Mater.* **2002**, *89*, 303–317. [[CrossRef](#)]
15. Shams-Ghahfarokhi, Z.; Nezamzadeh-Ejhi, A. As-synthesized ZSM-5 zeolite as a suitable support for increasing the photoactivity of semiconductors in a typical photodegradation process. *Mater. Sci. Semicond. Process.* **2015**, *39*, 265–275. [[CrossRef](#)]
16. Guillard, C.; Lachheb, H.; Houas, A.; Ksibi, M.; Elaloui, E.; Herrmann, J.-M. Influence of chemical structure of dyes, of pH and of inorganic salts on their photocatalytic degradation by TiO₂ comparison of the efficiency of powder and supported TiO₂. *J. Photochem. Photobiol. A Chem.* **2003**, *158*, 27–36. [[CrossRef](#)]
17. Akbal, F. Photocatalytic degradation of organic dyes in the presence of titanium dioxide under UV and solar light: Effect of operational parameters. *Environ. Prog.* **2005**, *24*, 317–322. [[CrossRef](#)]
18. Harish, S.; Archana, J.; Navaneethan, M.; Ponnusamy, S.; Singh, A.; Gupta, V.; Aswal, D.K.; Ikeda, H.; Hayakawa, Y. Synergetic effect of CuS@ZnS nanostructures on photocatalytic degradation of organic pollutant under visible light irradiation. *RSC Adv.* **2017**, *7*, 34366–34375. [[CrossRef](#)]
19. Zhang, W.; Sun, Y.; Xiao, Z.; Li, W.; Li, B.; Huang, X.; Liu, X.; Hu, J. Heterostructures of CuS nanoparticle/ZnO nanorod arrays on carbon fibers with improved visible and solar light photocatalytic properties. *J. Mater. Chem. A* **2015**, *3*, 7304–7313. [[CrossRef](#)]
20. Shafi, P.M.; Dhanabal, R.; Chithambararaj, A.; Velmathi, S.; Bose, A.C. α -MnO₂/h-MoO₃ Hybrid Material for High Performance Supercapacitor Electrode and Photocatalyst. *ACS Sustain. Chem. Eng.* **2017**, *5*, 4757–4770. [[CrossRef](#)]
21. Jing, Q.; Feng, X.; Zhao, X.; Duan, Z.; Pan, J.; Chen, L.; Liu, Y. Bi/BiVO₄ Chainlike Hollow Microstructures: Synthesis, Characterization, and Application as Visible-Light-Active Photocatalysts. *ACS Appl. Nano Mater.* **2018**, *1*, 2653–2661. [[CrossRef](#)]
22. Cho, I.-S.; Kim, D.W.; Lee, S.; Kwak, C.H.; Bae, S.-T.; Noh, J.H.; Yoon, S.H.; Jung, H.S.; Kim, D.-W.; Hong, K.S. Synthesis of Cu₂PO₄OH Hierarchical Superstructures with Photocatalytic Activity in Visible Light. *Adv. Funct. Mater.* **2008**, *18*, 2154–2162. [[CrossRef](#)]
23. Bi, Y.; Ouyang, S.; Umezawa, N.; Cao, J.; Ye, J. Facet Effect of Single-Crystalline Ag₃PO₄ Sub-microcrystals on Photocatalytic Properties. *J. Am. Chem. Soc.* **2011**, *133*, 6490–6492. [[CrossRef](#)]
24. Cho, I.-S.; Kwak, C.H.; Kim, D.W.; Lee, S.; Hong, K.S. Photophysical, Photoelectrochemical, and Photocatalytic Properties of Novel SnWO₄ Oxide Semiconductors with Narrow Band Gaps. *J. Phys. Chem. C* **2009**, *113*, 10647–10653. [[CrossRef](#)]
25. Yang, X.; Cui, H.; Li, Y.; Qin, J.; Zhang, R.; Tang, H. Fabrication of Ag₃PO₄-Graphene Composites with Highly Efficient and Stable Visible Light Photocatalytic Performance. *ACS Catal.* **2013**, *3*, 363–369. [[CrossRef](#)]
26. Clarke, E.A.; Anliker, R. Organic Dyes and Pigments. In *Anthropogenic Compounds. The Handbook of Environmental Chemistry*; Springer: Berlin/Heidelberg, Germany, 1980; Volume 3/3A, pp. 181–215.
27. Demirbas, A. Agricultural based activated carbons for the removal of dyes from aqueous solutions: A review. *J. Hazard. Mater.* **2009**, *167*, 1–9. [[CrossRef](#)]
28. Ramesha, G.K.; Vijaya Kumara, A.; Muralidhara, H.B.; Sampath, S. Graphene and graphene oxide as effective adsorbents toward anionic and cationic dyes. *J. Colloid Interface Sci.* **2011**, *361*, 270–277. [[CrossRef](#)]
29. Mishra, G.; Tripathy, M. A Critical Review of the Treatments for Decolourization of Textile Effluent. *Colourage* **1993**, *40*, 35–38.
30. Singhal, G.S.; Rabinowitch, E. Changes in the absorption spectrum of methylene blue with pH. *J. Phys. Chem.* **1967**, *71*, 3347–3349. [[CrossRef](#)]
31. Xu, B.; Wang, X.; Zhu, C.; Ran, X.; Li, T.; Guo, L. Probing the inhomogeneity and intermediates in the photosensitized degradation of rhodamine B by Ag₃PO₄ nanoparticles from an ensemble to a single molecule approach. *RSC Adv.* **2017**, *7*, 40896–40904. [[CrossRef](#)]

32. Guo, X.; Zhu, H.; Li, Q. Visible-light-driven photocatalytic properties of ZnO/ZnFe₂O₄ core/shell nanocable arrays. *Appl. Catal. B Environ.* **2014**, *160*, 408–414. [[CrossRef](#)]
33. Xing, Y.; Que, W.; Liu, X.; Javed, H.A.; He, Z.; He, Y.; Zhou, T. Bi₂Sn₂O₇-TiO₂ nanocomposites for enhancing visible light photocatalytic activity. *RSC Adv.* **2014**, *4*, 49900–49907. [[CrossRef](#)]
34. Choi, Y.I.; Kim, Y.-I.; Cho, D.W.; Kang, J.-S.; Leung, K.; Sohn, Y. Recyclable magnetic CoFe₂O₄/BiOX (X = Cl, Br and I) microflowers for photocatalytic treatment of water contaminated with methyl orange, rhodamine B, methylene blue, and a mixed dye. *RSC Adv.* **2015**, *5*, 79624–79634. [[CrossRef](#)]
35. Chen, C.; Lu, C.; Chung, Y.; Jan, J. UV light induced photodegradation of malachite green on TiO₂ nanoparticles. *J. Hazard. Mater.* **2007**, *141*, 520–528. [[CrossRef](#)]
36. Lee, S.-K.; Mills, A.; Lepre, A. An intelligence ink for oxygen. *Chem. Commun.* **2004**, 1912–1913. [[CrossRef](#)]
37. Lee, S.-K.; Sheridan, M.; Mills, A. Novel UV-activated colorimetric oxygen indicator. *Chem. Mater.* **2005**, *17*, 2744–2751. [[CrossRef](#)]
38. Wang, W.; Ye, M.; He, L.; Yin, Y. Nanocrystalline TiO₂-catalyzed photoreversible color switching. *Nano Lett.* **2014**, *14*, 1681–1686. [[CrossRef](#)]
39. Pan, M.; Zhang, H.; Gao, G.; Liu, L.; Chen, W. Facet-Dependent Catalytic Activity of Nanosheet-Assembled Bismuth Oxyiodide Microspheres in Degradation of Bisphenol A. *Environ. Sci. Technol.* **2015**, *49*, 6240–6248. [[CrossRef](#)]
40. Zhao, W.; Chen, C.; Li, X.; Zhao, J.; Hidaka, H.; Serpone, N. Photodegradation of Sulforhodamine-B Dye in Platinized Titania Dispersions under Visible Light Irradiation: Influence of Platinum as a Functional Co-catalyst. *J. Phys. Chem. B* **2002**, *106*, 5022–5028. [[CrossRef](#)]
41. Mahdiani, M.; Soofivand, F.; Ansari, F.; Salavati-Niasari, M. Grafting of CuFe₁₂O₁₉ nanoparticles on CNT and graphene: Eco-friendly synthesis, characterization and photocatalytic activity. *J. Clean. Prod.* **2018**, *176*, 1185–1197. [[CrossRef](#)]
42. Khorshidi, N.; Khorrami, S.; Olya, M.; Mottiee, F. Photodegradation of Basic Dyes using Nanocomposite (Silver Zinc Oxide-Copper Oxide) and Kinetic Studies. *Orient. J. Chem.* **2016**, *32*, 1205–1214. [[CrossRef](#)]
43. Vasanth Kumar, K.; Porkodi, K.; Selvaganapathi, A. Constrain in solving Langmuir-Hinshelwood kinetic expression for the photocatalytic degradation of Auramine O aqueous solutions by ZnO catalyst. *Dyes Pigments* **2007**, *75*, 246–249. [[CrossRef](#)]
44. Bora, T.; Zoepfl, D.; Dutta, J. Importance of Plasmonic Heating on Visible Light Driven Photocatalysis of Gold Nanoparticle Decorated Zinc Oxide Nanorods. *Sci. Rep.* **2016**, *6*, 26913. [[CrossRef](#)]
45. Han, A.; Sun, J.; Chuah, G.K.; Jaenicke, S. Enhanced p-cresol photodegradation over BiOBr/Bi₂O₃ in the presence of rhodamine B. *RSC Adv.* **2017**, *7*, 145–152. [[CrossRef](#)]
46. Tsui, S.M.; Chu, W. Quantum yield study of the photodegradation of hydrophobic dyes in the presence of acetone sensitizer. *Chemosphere* **2001**, *44*, 17–22. [[CrossRef](#)]
47. Nawrocka, A.; Krawczyk, S. Electronic Excited State of Alizarin Dye Adsorbed on TiO₂ Nanoparticles: A Study by Electroabsorption (Stark Effect) Spectroscopy. *J. Phys. Chem. C* **2008**, *112*, 10233–10241. [[CrossRef](#)]
48. Zhao, D.; Chen, C.; Wang, Y.; Ma, W.; Zhao, J.; Rajh, T.; Zang, L. Enhanced Photocatalytic Degradation of Dye Pollutants under Visible Irradiation on Al(III)-Modified TiO₂: Structure, Interaction, and Interfacial Electron Transfer. *Environ. Sci. Technol.* **2008**, *42*, 308–314. [[CrossRef](#)]
49. Chen, F.; Zhao, E.; Kim, T.; Wang, J.; Hableel, G.; Reardon, P.J.T.; Ananthakrishna, S.J.; Wang, T.; Arconada-Alvarez, S.; Knowles, J.C.; et al. Organosilica Nanoparticles with an Intrinsic Secondary Amine: An Efficient and Reusable Adsorbent for Dyes. *ACS Appl. Mater. Interfaces* **2017**, *9*, 15566–15576. [[CrossRef](#)]
50. Li, L.; Chen, W.; Li, X. Efficient adsorption of Norfloxacin by Fe-MCM-41 molecular sieves: Kinetic, isotherm and thermodynamic studies. *Chem. Eng. J.* **2015**, *281*, 397–403.
51. Dai, Y.; Zhang, K.; Li, J.; Jiang, Y.; Chen, Y.; Tanaka, S. Adsorption of copper and zinc onto carbon material in an aqueous solution oxidized by ammonium peroxydisulphate. *Sep. Purif. Technol.* **2017**, *186*, 255–263. [[CrossRef](#)]
52. Hu, Y.; Guo, T.; Ye, X.; Li, Q.; Guo, M.; Liu, H.; Wu, Z. Dye adsorption by resins: Effect of ionic strength on hydrophobic and electrostatic interactions. *Chem. Eng. J.* **2013**, *228*, 392–397. [[CrossRef](#)]
53. Cheng, F.; Wang, H.; Dong, X. The amphoteric properties of g-C₃N₄ nanosheets and fabrication of their relevant heterostructure photocatalysts by an electrostatic re-assembly route. *Chem. Commun.* **2015**, *51*, 7176–7179. [[CrossRef](#)]

54. Poullos, I.; Avranas, A.; Rekliti, E.; Zouboulis, A. Photocatalytic oxidation of Auramine O in the presence of semiconducting oxides. *J. Chem. Technol. Biotechnol.* **2000**, *75*, 205–212. [[CrossRef](#)]
55. Faria, P.C.C.; Órfão, J.J.M.; Pereira, M.F.R. Adsorption of anionic and cationic dyes on activated carbons with different surface chemistries. *Water Res.* **2004**, *38*, 2043–2052. [[CrossRef](#)]
56. Chun, H.; Yizhong, W.; Hongxiao, T. Influence of adsorption on the photodegradation of various dyes using surface bond-conjugated TiO₂/SiO₂ photocatalyst. *Appl. Catal. B Environ.* **2001**, *35*, 95–105. [[CrossRef](#)]
57. Bourikas, K.; Styliidi, M.; Kondarides, D.I.; Verykios, X.E. Adsorption of Acid Orange 7 on the Surface of Titanium Dioxide. *Langmuir* **2005**, *21*, 9222–9230. [[CrossRef](#)]
58. Kansal, S.K.; Kaur, N.; Singh, S. Photocatalytic Degradation of Two Commercial Reactive Dyes in Aqueous Phase Using Nanophotocatalysts. *Nanoscale Res. Lett.* **2009**, *4*, 709. [[CrossRef](#)]
59. Baran, W.; Makowski, A.; Wardas, W. The effect of UV radiation absorption of cationic and anionic dye solutions on their photocatalytic degradation in the presence TiO₂. *Dyes Pigments* **2008**, *76*, 226–230. [[CrossRef](#)]
60. Devi, L.G.; Kumar, S.G. Exploring the critical dependence of adsorption of various dyes on the degradation rate using Ln³⁺-TiO₂ surface under UV/solar light. *Appl. Surf. Sci.* **2012**, *261*, 137–146. [[CrossRef](#)]
61. Zajac, K.; Choina, J.; Dolat, D.; Morawski, A. Methylene Blue and Phenol Photocatalytic Degradation on Nanoparticles of Anatase TiO₂. *Pol. J. Environ. Stud.* **2010**, *19*, 685–691.
62. Fan, Y.; Liu, H.-J.; Zhang, Y.; Chen, Y. Adsorption of anionic MO or cationic MB from MO/MB mixture using polyacrylonitrile fiber hydrothermally treated with hyperbranched polyethylenimine. *J. Hazard. Mater.* **2015**, *283*, 321–328. [[CrossRef](#)]
63. Zhao, H.; Zhang, Y.; Li, G.; Tian, F.; Tang, H.; Chen, R. Rhodamine B-sensitized BiOCl hierarchical nanostructure for methyl orange photodegradation. *RSC Adv.* **2016**, *6*, 7772–7779. [[CrossRef](#)]
64. Kong, J.-Z.; Li, A.-D.; Li, X.-Y.; Zhai, H.-F.; Zhang, W.-Q.; Gong, Y.-P.; Li, H.; Wu, D. Photo-degradation of methylene blue using Ta-doped ZnO nanoparticle. *J. Solid State Chem.* **2010**, *183*, 1359–1364. [[CrossRef](#)]
65. Gomathi Devi, L.; Narasimha Murthy, B.; Girish Kumar, S. Heterogeneous photo catalytic degradation of anionic and cationic dyes over TiO₂ and TiO₂ doped with Mo⁶⁺ ions under solar light: Correlation of dye structure and its adsorptive tendency on the degradation rate. *Chemosphere* **2009**, *76*, 1163–1166. [[CrossRef](#)]
66. Saquib, M.; Muneer, M. TiO₂-mediated photocatalytic degradation of a triphenylmethane dye (gentian violet), in aqueous suspensions. *Dyes Pigments* **2003**, *56*, 37–49. [[CrossRef](#)]
67. Kumar, A.; Kumar, R.; Pandey, G. Synthesis, Characterization of Titania/Polyaniline/GO Nanocomposites, and Its Photocatalytic Activity Under UV-Visible Light. *Macromol. Symp.* **2018**, *379*, 1600192. [[CrossRef](#)]
68. Giwa, A.; Nkeonye, P.O.; Bello, K.A.; Kolawole, E.G.; Campos, A.O. Solar Photocatalytic Degradation of Reactive Yellow 81 and Reactive Violet 1 in Aqueous Solution Containing Semiconductor Oxides. *Int. J. Appl. Sci. Technol.* **2012**, *2*, 90–105.
69. Saggiaro, E.; Oliveira, A.; Pavesi, T.; Maia, C.; Vieira Ferreira, L.F.; Moreira, J. Use of Titanium Dioxide Photocatalysis on the Remediation of Model Textile Wastewaters Containing Azo Dyes. *Molecules* **2011**, *16*, 10370–10386. [[CrossRef](#)]
70. Boruah, P.K.; Borthakur, P.; Darabdhara, G.; Kamaja, C.K.; Karbhal, I.; Shelke, M.V.; Phukan, P.; Saikia, D.; Das, M.R. Sunlight assisted degradation of dye molecules and reduction of toxic Cr(vi) in aqueous medium using magnetically recoverable Fe₃O₄/reduced graphene oxide nanocomposite. *RSC Adv.* **2016**, *6*, 11049–11063. [[CrossRef](#)]
71. Kiriakidou, F.; Kondarides, D.I.; Verykios, X.E. The effect of operational parameters and TiO₂-doping on the photocatalytic degradation of azo-dyes. *Catal. Today* **1999**, *54*, 119–130. [[CrossRef](#)]
72. Nam, W.; Kim, J.; Han, G. Photocatalytic oxidation of methyl orange in a three-phase fluidized bed reactor. *Chemosphere* **2002**, *47*, 1019–1024. [[CrossRef](#)]
73. Kundu, S.; Pal, A.; Dikshit, A.K. UV induced degradation of herbicide 2,4-D: Kinetics, mechanism and effect of various conditions on the degradation. *Sep. Purif. Technol.* **2005**, *44*, 121–129. [[CrossRef](#)]
74. Sun, P.; Zhang, J.; Liu, W.; Wang, Q.; Cao, W. Modification to L-H Kinetics Model and Its Application in the Investigation on Photodegradation of Gaseous Benzene by Nitrogen-Doped TiO₂. *Catalysts* **2018**, *8*, 326. [[CrossRef](#)]
75. Ollis, D.F.; Pelizzetti, E.; Serpone, N. Photocatalyzed destruction of water contaminants. *Environ. Sci. Technol.* **1991**, *25*, 1522–1529. [[CrossRef](#)]

76. Mehrotra, K.; Yablonsky, G.S.; Ray, A.K. Macro kinetic studies for photocatalytic degradation of benzoic acid in immobilized systems. *Chemosphere* **2005**, *60*, 1427–1436. [[CrossRef](#)]
77. Hashimoto, K.; Irie, H.; Fujishima, A. TiO₂ Photocatalysis: A Historical Overview and Future Prospects. *Jpn. J. Appl. Phys.* **2005**, *44*, 8269–8285. [[CrossRef](#)]
78. Barakat, N.A.M.; Kanjwal, M.A.; Chronakis, I.S.; Kim, H.Y. Influence of temperature on the photodegradation process using Ag-doped TiO₂ nanostructures: Negative impact with the nanofibers. *J. Mol. Catal. A Chem.* **2013**, *366*, 333–340. [[CrossRef](#)]
79. Yang, T.-T.; Chen, W.-T.; Hsu, Y.-J.; Wei, K.-H.; Lin, T.-Y.; Lin, T.-W. Interfacial Charge Carrier Dynamics in Core–Shell Au–CdS Nanocrystals. *J. Phys. Chem. C* **2010**, *114*, 11414–11420. [[CrossRef](#)]
80. Lin, W.-H.; Chiu, Y.-H.; Shao, P.-W.; Hsu, Y.-J. Metal-Particle-Decorated ZnO Nanocrystals: Photocatalysis and Charge Dynamics. *ACS Appl. Mater. Interfaces* **2016**, *8*, 32754–32763. [[CrossRef](#)]
81. Lin, Y.-F.; Hsu, Y.-J. Interfacial charge carrier dynamics of type-II semiconductor nanoheterostructures. *Appl. Catal. B Environ.* **2013**, *130–131*, 93–98. [[CrossRef](#)]
82. Chen, M.-Y.; Hsu, Y.-J. Type-II nanorod heterostructure formation through one-step cation exchange. *Nanoscale* **2013**, *5*, 363–368. [[CrossRef](#)]
83. Chen, Y.-C.; Pu, Y.-C.; Hsu, Y.-J. Interfacial Charge Carrier Dynamics of the Three-Component In₂O₃–TiO₂–Pt Heterojunction System. *J. Phys. Chem. C* **2012**, *116*, 2967–2975. [[CrossRef](#)]
84. Pu, Y.-C.; Chou, H.-Y.; Kuo, W.-S.; Wei, K.-H.; Hsu, Y.-J. Interfacial charge carrier dynamics of cuprous oxide-reduced graphene oxide (Cu₂O-rGO) nanoheterostructures and their related visible-light-driven photocatalysis. *Appl. Catal. B Environ.* **2017**, *204*, 21–32. [[CrossRef](#)]
85. Chiu, Y.-H.; Hsu, Y.-J. Au@Cu₇S₄ yolk@shell nanocrystal-decorated TiO₂ nanowires as an all-day-active photocatalyst for environmental purification. *Nano Energy* **2017**, *31*, 286–295. [[CrossRef](#)]
86. Naresh, G.; Hsieh, P.-L.; Meena, V.; Lee, S.-K.; Chiu, Y.-H.; Madasu, M.; Lee, A.-T.; Tsai, H.-Y.; Lai, T.-H.; Hsu, Y.-J.; et al. Facet-Dependent Photocatalytic Behaviors of ZnS-Decorated Cu₂O Polyhedra Arising from Tunable Interfacial Band Alignment. *ACS Appl. Mater. Interfaces* **2019**, *11*, 3582–3589. [[CrossRef](#)]
87. Pu, Y.-C.; Lin, W.-H.; Hsu, Y.-J. Modulation of charge carrier dynamics of Na_xH_{2–x}Ti₃O₇–Au–Cu₂O Z-scheme nanoheterostructures through size effect. *Appl. Catal. B Environ.* **2015**, *163*, 343–351. [[CrossRef](#)]
88. Chen, F.; Deng, Z.; Li, X.; Zhang, J.; Zhao, J. Visible light detoxification by 2,9,16,23-tetracarboxyl phthalocyanine copper modified amorphous titania. *Chem. Phys. Lett.* **2005**, *415*, 85–88. [[CrossRef](#)]
89. Yan, S.C.; Li, Z.S.; Zou, Z.G. Photodegradation of Rhodamine B and Methyl Orange over Boron-Doped g-C₃N₄ under Visible Light Irradiation. *Langmuir* **2010**, *26*, 3894–3901. [[CrossRef](#)]
90. Cao, R.; Yang, H.; Deng, X.; Zhang, S.; Xu, X. In-situ synthesis of amorphous silver silicate/carbonate composites for selective visible-light photocatalytic decomposition. *Sci. Rep.* **2017**, *7*, 15001. [[CrossRef](#)]
91. Qiu, P.; Chen, H.; Xu, C.; Zhou, N.; Jiang, F.; Wang, X.; Fu, Y. Fabrication of an exfoliated graphitic carbon nitride as a highly active visible light photocatalyst. *J. Mater. Chem. A* **2015**, *3*, 24237–24244. [[CrossRef](#)]
92. Xu, T.; Zhang, L.; Cheng, H.; Zhu, Y. Significantly enhanced photocatalytic performance of ZnO via graphene hybridization and the mechanism study. *Appl. Catal. B Environ.* **2011**, *101*, 382–387. [[CrossRef](#)]
93. Tian, Y.; Chang, B.; Yang, Z.; Zhou, B.; Xi, F.; Dong, X. Graphitic carbon nitride–BiVO₄ heterojunctions: Simple hydrothermal synthesis and high photocatalytic performances. *RSC Adv.* **2014**, *4*, 4187–4193. [[CrossRef](#)]
94. Teng, W.; Li, X.; Zhao, Q.; Zhao, J.; Zhang, D. In situ capture of active species and oxidation mechanism of RhB and MB dyes over sunlight-driven Ag/Ag₃PO₄ plasmonic nanocatalyst. *Appl. Catal. B Environ.* **2012**, *125*, 538–545. [[CrossRef](#)]
95. Hu, Y.; Li, D.; Wang, H.; Zeng, G.; Li, X.; Shao, Y. Role of active oxygen species in the liquid-phase photocatalytic degradation of RhB using BiVO₄/TiO₂ heterostructure under visible light irradiation. *J. Mol. Catal. A Chem.* **2015**, *408*, 172–178. [[CrossRef](#)]
96. Hou, J.; Jiang, K.; Shen, M.; Wei, R.; Wu, X.; Idrees, F.; Cao, C. Micro and nano hierarchical structures of BiOI/activated carbon for efficient visible-light-photocatalytic reactions. *Sci. Rep.* **2017**, *7*, 11665. [[CrossRef](#)]
97. Jiang, Y.-R.; Lin, H.-P.; Chung, W.-H.; Dai, Y.-M.; Lin, W.-Y.; Chen, C.-C. Controlled hydrothermal synthesis of BiOxCly/BiOmIn composites exhibiting visible-light photocatalytic degradation of crystal violet. *J. Hazard. Mater.* **2015**, *283*, 787–805. [[CrossRef](#)]
98. Chou, S.-Y.; Chung, W.-H.; Chen, L.-W.; Dai, Y.-M.; Lin, W.-Y.; Lin, J.-H.; Chen, C.-C. A series of BiO_xI_y/GO photocatalysts: Synthesis, characterization, activity, and mechanism. *RSC Adv.* **2016**, *6*, 82743–82758. [[CrossRef](#)]

99. Liu, X.; Zhang, T.; Xu, D.; Zhang, L. Microwave-Assisted Catalytic Degradation of Crystal Violet with Barium Ferrite Nanomaterial. *Ind. Eng. Chem. Res.* **2016**, *55*, 11869–11877. [[CrossRef](#)]
100. Liu, X.; An, S.; Shi, W.; Yang, Q.; Zhang, L. Microwave-induced catalytic oxidation of malachite green under magnetic Cu-ferrites: New insight into the degradation mechanism and pathway. *J. Mol. Catal. A Chem.* **2014**, *395*, 243–250. [[CrossRef](#)]
101. Arifin, S.A.; Jalaludin, S.; Saleh, R. Photocatalytic Decolorization of Malachite Green in the Presence of Fe₃O₄/TiO₂/CuO Nanocomposites. *Mater. Sci. Forum* **2015**, *1123*, 264–269.
102. Kulsi, C.; Ghosh, A.; Mondal, A.; Kargupta, K.; Ganguly, S.; Banerjee, D. Remarkable photo-catalytic degradation of malachite green by nickel doped bismuth selenide under visible light irradiation. *Appl. Surf. Sci.* **2017**, *392*, 540–548. [[CrossRef](#)]
103. Kushwaha, H.; Vaish, R. Enhanced Visible Light Photocatalytic Activity of Curcumin-Sensitized Perovskite Bi_{0.5}Na_{0.5}TiO₃ for Rhodamine 6G Degradation. *Int. J. Appl. Ceram. Technol.* **2015**, *13*, 333–339. [[CrossRef](#)]
104. Mohapatra, L.; Parida, K.; Satpathy, M. Molybdate/Tungstate Intercalated Oxo-Bridged Zn/Y LDH for Solar Light Induced Photodegradation of Organic Pollutants. *J. Phys. Chem. C* **2012**, *116*, 13063–13070. [[CrossRef](#)]
105. Kaur, R.; Vellingiri, K.; Kim, K.-H.; Paul, A.K.; Deep, A. Efficient photocatalytic degradation of rhodamine 6G with a quantum dot-metal organic framework nanocomposite. *Chemosphere* **2016**, *154*, 620–627. [[CrossRef](#)]
106. Chen, Y.; Yang, S.; Wang, K.; Lou, L. Role of primary active species and TiO₂ surface characteristic in UV-illuminated photodegradation of Acid Orange 7. *J. Photochem. Photobiol. A Chem.* **2005**, *172*, 47–54. [[CrossRef](#)]
107. Li, G.; Wong, K.H.; Zhang, X.; Hu, C.; Yu, J.C.; Chan, R.C.Y.; Wong, P.K. Degradation of Acid Orange 7 using magnetic AgBr under visible light: The roles of oxidizing species. *Chemosphere* **2009**, *76*, 1185–1191. [[CrossRef](#)]
108. Reza Pouretedal, H.; Hosseini, M. Bleaching Kinetic and Mechanism Study of Congo Red Catalyzed by ZrO₂ Nanoparticles Prepared by Using a Simple Precipitation Method. *Acta Chim. Slov.* **2010**, *57*, 415–423.
109. Bhoi, Y.P.; Pradhan, S.R.; Behera, C.; Mishra, B.G. Visible light driven efficient photocatalytic degradation of Congo red dye catalyzed by hierarchical CuS-Bi₂Cu_xW_{1-x}O_{6-2x} nanocomposite system. *RSC Adv.* **2016**, *6*, 35589–35601. [[CrossRef](#)]
110. Paramarta, V.; Taufik, A.; Munisa, L.; Saleh, R. Sono- and photocatalytic activities of SnO₂ nanoparticles for degradation of cationic and anionic dyes. *AIP Conf. Proc.* **2017**, *1788*, 030125. [[CrossRef](#)]
111. Kaur, S.; Sharma, S.; Kansal, S.K. Synthesis of ZnS/CQDs nanocomposite and its application as a photocatalyst for the degradation of an anionic dye, ARS. *Superlattices Microstruct.* **2016**, *98*, 86–95. [[CrossRef](#)]
112. Ghugal, S.G.; Umare, S.S.; Sasikala, R. Photocatalytic mineralization of anionic dyes using bismuth doped CdS-Ta₂O₅ composite. *RSC Adv.* **2015**, *5*, 63393–63400. [[CrossRef](#)]
113. Song, S.; Xu, L.; He, Z.; Chen, J.; Xiao, X.; Yan, B. Mechanism of the Photocatalytic Degradation of C.I. Reactive Black 5 at pH 12.0 Using SrTiO₃/CeO₂ as the Catalyst. *Environ. Sci. Technol.* **2007**, *41*, 5846–5853. [[CrossRef](#)]
114. Roushani, M.; Mavaei, M.; Rajabi, H.R. Graphene quantum dots as novel and green nano-materials for the visible-light-driven photocatalytic degradation of cationic dye. *J. Mol. Catal. A Chem.* **2015**, *409*, 102–109. [[CrossRef](#)]
115. Guo, J.; Liao, X.; Lee, M.-H.; Hyett, G.; Huang, C.-C.; Hewak, D.W.; Mailis, S.; Zhou, W.; Jiang, Z. Experimental and DFT insights of the Zn-doping effects on the visible-light photocatalytic water splitting and dye decomposition over Zn-doped BiOBr photocatalysts. *Appl. Catal. B Environ.* **2019**, *243*, 502–512. [[CrossRef](#)]
116. Trandafilović, L.V.; Jovanović, D.J.; Zhang, X.; Ptasińska, S.; Dramićanin, M.D. Enhanced photocatalytic degradation of methylene blue and methyl orange by ZnO:Eu nanoparticles. *Appl. Catal. B Environ.* **2017**, *203*, 740–752. [[CrossRef](#)]

117. Chen, J.; Wang, H.; Huang, G.; Zhang, Z.; Han, L.; Song, W.; Li, M.; Zhang, Y. Facile synthesis of urchin-like hierarchical Nb₂O₅ nanospheres with enhanced visible light photocatalytic activity. *J. Alloy. Compd.* **2017**, *728*, 19–28. [[CrossRef](#)]
118. Ohtani, B. Preparing Articles on Photocatalysis—Beyond the Illusions, Misconceptions, and Speculation. *Chem. Lett.* **2008**, *37*, 216–229. [[CrossRef](#)]



© 2019 by the authors. Licensee MDPI, Basel, Switzerland. This article is an open access article distributed under the terms and conditions of the Creative Commons Attribution (CC BY) license (<http://creativecommons.org/licenses/by/4.0/>).